Lowermost mantle shear-velocity structure from hierarchical trans-dimensional Bayesian tomography

[1]S. Mousavi, [1]H. Tkalčić, [2]R. Hawkins, [1]M. Sambridge

1) Research School of Earth Sciences, The Australian National University, Canberra, ACT, Australia

2) Department of Earth Sciences, Utrecht University, Utrecht, Netherlands

Abstract

The core-mantle boundary (CMB) is the most extreme boundary within the Earth where the liquid, iron-rich outer core interacts with the rocky, silicate mantle. The nature of the lowermost mantle atop the CMB, and its role in mantle dynamics, is not completely understood. Various regional studies have documented significant heterogeneities at different spatial scales. While there is a consensus on the long scale-length structure of the inferred S-wave speed tomograms, there are also notable differences stemming from different imaging methods and datasets. Here we aim to overcome over-smoothing and avoid over-fitting data for the case where the spatial coverage is sparse and the inverse problem ill-posed. Here we present an S-wave tomography model at global scale for the Lowermost Mantle (LM) using the Hierarchical Trans-dimensional Bayesian Inversion (HTDBI) framework, LM-HTDBI. Our HTDBI analysis of ScS-S travel times includes uncertainty, and the complexity of the model is deduced from the data itself through an implicit parameterization of the model space. Our comprehensive resolution estimates indicate that short-scale anomalies are significant and resolvable features of the lowermost mantle regardless of the chosen mantle-model reference to correct the travel times above the D'' layer. The recovered morphology of the Large-Low-Shear-wave Velocity Provinces (LLSVPs) is complex, featuring small high-velocity patches among low-velocity domains. Instead of two large, unified, and smooth LLSVPs, the newly obtained images suggest that their margins are not uniformly flat.

Plain Language Summary

The lowermost mantle sits atop the core-mantle boundary - the most dramatic boundary within our planet, with contrasts in physical properties that exceed those that exist at the surface. Despite significant progress in recent years, this part of the Earth is not well understood, and various tomographic studies on global scale, along with regional studies that focus on seismic waveform modelling, pave the path towards higher resolution and new understanding. Important questions to answer are on the distribution, shape, size and composition of inhomogeneities in the lowermost mantle, and their critical role in mantle and core dynamics.
While there is a general consensus on the long-scale length structures inferred from long-period shear waves, there are notable differences in details of the tomograms of the lowermost mantle, stemming from the use of different imaging methods and datasets. Here, we utilize a large traveltime dataset of ScS and S waves with a significant addition of new measurements sensitive to the lowermost mantle to perform a probabilistic shear-wave tomography, and we retrieve a high-resolution image of the lowermost mantle. The new shear-wave speed tomogram and comprehensive resolution-estimations indicate that short and medium scale inhomogeneities are omnipresent features of the lowermost mantle.

1. Introduction

The core-mantle boundary (CMB) lies approximately halfway down to the Earth's center and is the boundary with the most extreme contrasts in seismic velocity, viscosity, and density, where the heat from the outer core is being transmitted to the mantle. This thermal boundary per se cannot explain the observation of isolated blobs of partial melt (Williams & Garnero, 1996; Li 2002; Suzuki et al. 2020) and sharp changes in seismic velocity and anisotropy (e.g. Wenk et al., 2011; Nawacki & Woodi 2016; Creasy et al., 2017) in the bottom 300-km part of the mantle, also known as D''. Geodynamical simulations show that mantle convection sweeps intrinsically hotter material towards upwelling regions (e.g. McNamara & Zhong, 2005) and alternatively, pushes the subducted slabs to the base of mantle (e.g. Ricard et al., 1993; Fukao et al. 2001). Therefore, the subduction history can potentially lead to the development of thermochemical heterogeneities in D''.

The two dominant features at the top of the CMB identified by seismic imaging of long-period S-waves are the so-called Large-Low-Shear-wave Velocity Provinces (LLSVPs), and they are situated roughly beneath Africa and the Pacific (e.g. Masters et al., 2000; Garnero and McNamara, 2008; Simmons et al., 2010) covering more than 25% of the CMB (e.g. Koelemeijer et al., 2017). The geographical position and overall shape of LLSVPs, as inferred from different tomographic models using various datasets and methods, are in a good general agreement, although differences are present with regards to the specific shape and lateral extension of LLSVP margins (eg. Garnero et al, 2016; Cottaar & Lekić, 2016). A recent geochemical analysis has shown that the two LLSVPs hold different evolutionary histories which are related to the assembly and breakup of the supercontinents, supporting a dynamic relationship between plate tectonics and the lowermost mantle structures (Doucet et al., 2020).

Apart from LLSVPs, past seismological studies that involve waveform modeling presented arguments for the existence of intermediate heterogeneity (e.g. Rost & Earle 2010; Wysession et al., 1994), sharp transitions (e.g. Ni and Helmberger, 2001), short-scale heterogeneity (e.g. Tkalčić and Romanowicz, 2002); as well as ultra-low-velocity zones (ULVZs) (e.g. Garnero and Helmberger, 1995; Avants et al., 2005; Thorne et al., 2013; Pachhai et al., 2014; McNamara, 2019). Recent studies by employing P-wave travel times that focused either solely on the lowermost mantle (Young et al., 2014; Tkalčić et al., 2015; Muir and Tkalčić, 2020) or the whole mantle (Hosseini et al., 2019) have indicated that the D'' is far more complex than what global S-wave studies revealed (e.g. Grand, 2002; Simmons et al., 2010; Moulik & Ekström 2014), with heterogeneity scales comparable to those found in the Earth's crust.

Importantly, while various regional studies have argued for the existence of short-scale heterogeneities (e.g. He & Wen 2011; Takeuchi, et al., 2008; Takeuchi 2012; Frost et al, 2013; Hung et al., 2005; Suzuki et al., 2020; Li et al., 2021) the global seismic studies of shear-waves robustly revealed a dominant character of long-scale features (e.g. Houser et al., 2008; Durand et al., 2017). A recent mantle model using shear waves, developed by French and Romanowicz (2014) utilized waveform inversion of selected windows of body waves (300 – 32 s) and surface waves (400 – 60 s) to provide a detailed image of the Earth's mantle. This model also found evidence for short-scale heterogeneity at the top of the CMB.

The remarkable diversity of the short and medium scale anomalies suggests a significant uncertainty amongst models, even at the scales that they allegedly resolve (e.g. Moulik and Ekström 2014; Kustowski et al., 2008; Simmons et al., 2010). In our hypothesis, most discrepancies among various tomographic models stem from the adopted procedures. First, they are prone to subjective choices of model parameters and regularization, which, in turn, determines the level of model complexity. In model regularizations, smoothing and damping are usually applied to the entire model, and consequently, they mute the sharp edges that are likely present in Earth and transform them into pixelated gradual transitions. Second, building models based on explicit parameterizations such as regular cells which ignores the spatial variability in the data's resolving power usually introduces small-scale artefacts in regions with less ray coverage. Third, the difficulty in quantifying data uncertainties takes its toll since the level of data noise is usually determined by the user, prior to the inversion, and it regulates the level of data fit.

To take a progressive approach and improve the imaging capability of structural features in the D'' by using travel times only, we believe it is essential to possess the following two ingredients: a) differential travel times of body waves, whose use suppresses the unwanted crustal and upper mantle effects near the source and receiver, thus capturing the contribution from the lowermost mantle, b) an improved theoretical and methodological framework to overcome the aforementioned limitations in various seismic-tomography inversion approaches. For this purpose, we use the Hierarchical Trans-dimensional Bayesian Inversion (HTDBI) framework to perform a tomographic inversion that circumvents subjective choices. In fact, the first global imaging application of the HTDBI method was to study the lowermost mantle (Young et al., 2013; Tkalčić et al. 2015), but the improvement here in comparison with the previous studies is that we now deploy truly-spherical Voronoi parameterization. This type of parameterization has recently been applied in an attenuation tomography (Pejić et at., 2019) and the P-wave velocity tomography studies of the upper inner core

(Burdick et al., 2019). The main limitation of our study (due to the computational expense consideration) is that we do not account for the finite frequency effects. In contrast, other global tomography studies have utilized more complete information by utilizing waveforms, a wide range of body waves and phases, and normal modes.

In subsequent Sections, we present a development of a new shear-wave velocity model of the D''. In Section 2, we explain the data that was used in the inversion. In Section 3, we discuss how the HTDBI method differs from the linearized travel-time tomography. Next, in Section 4, we present the resolution tests including an all-embracing test for an abstract, complex, D'' model and a test for a more realistic structure, which mimics the final pattern of anomalies in D''. In Section 5, we explain the inversion and data analysis that we carried out through HTDBI. In Section 6, we first describe our approach to correcting for mantle structure and then present the averaged shear-wave velocity model together with its standard deviation map. In Sections 7 and 8 we compare our model with other available models of D'' and discuss the advantages of using HTDBI in global imaging of D''.

2. Data

In this study, we utilize differential travel time of shear waves to image the heterogeneity pattern at the lowermost mantle. Differential travel times of body waves are particularly helpful: first, by reducing the unwanted crustal and upper mantle effects near the source and receiver, since the raypaths are close for the large epicentral distances in the crust and upper mantle; second, source mislocations are not projected into the model.

We used ScS-S differential travel times from Houser et al., (2008) which encompasses events from 1976 – 2007, and augmented it by our newly measured data in the time window 2008 – 2018, focusing on the source-receiver geometries that fill the gaps in spatial coverage of the Houser et al (2008) dataset. We considered only earthquakes with simple source-time functions and magnitudes $5.5<M<7.5$. To reduce the effect of upper mantle structure on our ScS-S data set, we imposed a relatively strict criterion and only selected the event-station pairs at epicentral distances between 60 and 75 degrees (Fig. 1a). In these epicentral distances, the raypaths of ScS and S waves are more proximate to each other and thus their differential travel time is a better proxy for the travel time affected by D'' structure where they differ the most. The vertical separation between the bottoming points of S and ScS varies from 1450 km to 950 km for epicentral distances of 60 and 75 degrees. Our data-selection procedure resulted in 18,131 rays in total, including 16,344 rays out of the

original 41,000 rays (Houser et al., 2008) indicated by the red dashed line in Fig. 1b, and the newly-collected 1,787 rays, to augment the geometric coverage and enhance the imaging capacity of D''. The resulting coverage of rays in CMB is shown in the top panel of Fig. 2 and the Supporting Information (Fig. S1). A simple calculation for our dataset shows that over 70% of the CMB has a hit count of 5 or more if we divide the area of CMB to 4 ° by 4 ° cells. The distribution of the bounce points of ScS rays and their raypaths for both datasets at the CMB are shown in Fig. 2b & 2c. We compare the newly picked data and dataset from Houser et al., (2008) in the Supporting Information (Fig. S2 to Fig. S3).

To ensure the compatibility between the two datasets we followed the same measurement technique as Houser et al., (2008) and handpicked the differential travel times through waveform correlation of band-pass filtered waveform data at 10–50 s (Fig. 3). Correspondingly, the size of the first Fresnel zone for ScS in the lowermost mantle is near 400 km in diameter, which can be interpreted as a rough approximation of the potential resolution of the data in the areas with intermediate or low coverage and a criterion for the size of resolved short-scale heterogeneities.

The advantage of handpicking is that it allows us to align the onsets of S and ScS phases and discard noisy waveforms. The measurements were made on transverse components to suppress any interference from converted phases.

Given the fact that S and ScS raypaths are not identical in the lower mantle (albeit they are similar), to further reduce the effects of mantle heterogeneity, S and ScS travel times were corrected for 3D mantle structure using 1D ray paths down to the top of D'' (300 km above CMB) using five global mantle models: TX2011 (Grand, 2002), S362ANI+M (Moulik and Ekström, 2014), GyPSuM-S (Simmons et al, 2010), SEMUCB-WM1 (French and Romanowicz, 2014) and SAW642ANb (Panning et al., 2010). S and ScS traced in the mantle using "tau-p" (Buland and Chapman, 1983) through PREM and the extracted mantle velocity structure (based on the selected five global models and their reference models) along each ray path give the time corrections for S and ScS. While this does not account for ray bending that might occur due to 3D structure, the difference between velocities sampled along 1D and 3D ray paths is minimal given the long wavelength of features imaged in tomographic models. Mantle correction reasonably suppresses the projection of mantle heterogeneities into the inferred structure of D''. At these epicentral distances and in the crust, the raypaths of S and ScS are nearly identical, which means that the correction for the crust is not necessary. The corrected ScS-S data from all 5 models are then inverted for the velocity anomalies in D''.

3. Method

We employed the HTDBI method (Bodin et al., 2012; Young et al., 2013; Pejić et al., 2019) as our preferred inversion method to image the lowermost mantle. The HTDBI method includes the overall level of data noise as a free parameter in the inversion process, together with the number of model parameters. Consequently, large, small, smooth, and sharp discontinuous features can be resolved based on the trade-off between data uncertainty and resolution. In the non-HTDBI tomographic inversions, arbitrary choices, such as a single parameterization type, damping, and smoothing, must be made a priori. These choices can be especially problematic in global seismic tomography, where an uneven distribution of sources and receivers causes uneven ray coverage. Also, the use of a fixed regular grid of some chosen size typically introduces artifacts in regions of low ray coverage, where the particular property being investigated is poorly constrained.

Here, we assume a 300-km-thick layer atop CMB to perform the inversion. The choice of 300 km is based on the average thickness of D'' (350±50 km) presented by statistical analysis of Garcia et al. (2009) and empirical examination of different D'' thicknesses in Tkalčić et al. (2015). Given the trade-off between layer thickness and the amplitude of perturbations, further advances will include the HTDBI approaches where the thickness and the amplitude of the perturbation will be treated as variables.

The Trans-dimensional inverse problem in tomography may be solved with the reversible jump algorithm (Bodin et al., 2012) in which the solution is represented by multi-scale irregular ensemble of Voronoi cells with variable number and size (see Supporting information, Fig. S5 for example of a Voronoi model). For a review of the trans-dimensional Bayesian inference, see a review of Sambridge et al. (2013). In this approach, the Voronoi cells dynamically change their position, values (here velocity) and number (via death and birth of the cells) during the inversion, within the context of multi-dimensional probabilistic sampling.

Bayes' theorem is applied to solve the inverse problem in which the solution is represented as a posterior probability distribution. The Bayes' theorem for a trans-dimensional model can be represented as:

$$p(m,k|d) \propto p(d|m,k) \times p(m|k)p(k) \qquad (1)$$

where m is the model and d is the observed data, $p(d|m,k)$ is the likelihood term, $p(m|k)$ is the prior Probability Distribution Function (PDF) for model m given k, $p(k)$ is the prior on k, the number of Voronoi cells, typically chosen to be uniform between chosen limits.

The Likelihood term includes the forward modeling, where we make predictions of travel times for a given Earth model. Here, the forward model involves computation of a travel time prediction along each ray path in D'' using the tau-p algorithm through the PREM Earth model (Dziewonski and Anderson, 1981). The accrued time differences between the 1D and 2D ray-tracing are on the same order of magnitude as the uncertainty introduced by ray tracing through various mantle tomographic models (up to several seconds for most extreme velocity perturbations). Still, moving from 1D to 2D or complete 3D ray tracing is an ambitious computational goal within the HTDBI framework, which hopefully the next generation of models will achieve.

The downward and upward ray-legs of ScS in D'' layer with 300 km thickness are projected along with the longitude and latitude coordinates on the surface of a sphere. The predicted travel times of ScS are attributed to the surface projection of ScS ray path on the D'' spherical shell. The prediction is then compared to the observation. We assume travel time errors are independently and normally distributed which leads to a Gaussian likelihood of the following form:

$$L = p(d|m) = \frac{1}{\sqrt{2\pi}\Pi_{i=1}^{N}\sigma_i} e^{-\sum_{i=1}^{N}\frac{(G(m)_i - d_i)^2}{2{\sigma_i}^2}} \qquad (2)$$

where $G(m)$ is data predicted from model m, d_i is observation, N is the total number of observations and σ_i is the error of the observation. The negative log-likelihood, $-log(L)$, is a measure of data misfit used by the algorithm. Minimizing the negative log-likelihood is equivalent to maximizing the posterior probability.

In the hierarchical approach, the data noise, σ_i, is assumed a fixed parameter and a scaling hierarchical parameter, λ, is allowed to vary. Together, they define the noise parameter, $\sigma_{N,i}$:

$$\sigma_{N,i} = \sigma_i . \lambda \qquad (3)$$

A Bayesian setting is adopted to solve the inverse problem in which the solution is represented as a posterior probability distribution over a multi-dimensional Earth model, m (the first term in eq. 1). An ensemble of models generated with the Birth-Death Markov chain Monte Carlo, McMC, (Geyer

and Moyer, 1994), which is a special case of the generalized reversible jump algorithm (Green, 1995).

The McMC algorithm probabilistically samples Earth models, with variable numbers of unknowns, in proportion to their support as expressed by the combination of the likelihood and prior. The property known as natural parsimony ensures more complex, higher k models, which, if optimized, would fit the data better, but are not necessarily favored over less complex, lower k, models (Mackay, 2003). In the McMC algorithm, new models are proposed according to some chosen proposal distribution, and these get accepted or rejected probabilistically according to an acceptance ratio. Typically a Gaussian proposal PDF width for velocity perturbations is adjusted so that actual acceptance levels are between 30 – 50% (Tarantola, 2005). If acceptance levels are much lower than this then the algorithm spends a large proportion of time-solving the forward problem for models that are ultimately rejected. This is often the case when the proposal step size is too large. If acceptance levels much higher than this range are obtained, the algorithm is likely inefficiently walking through model space taking small steps and thereby sampling many similar models. The acceptance rate between 30 – 50% is where the random walk establishes a balance between large and small steps.

By definition, each new model (or step) along a Markov chain is dependent on the previous step. Since each chain is typically initiated at an arbitrary point in model space, which may be poorly supported by the data, (i.e. having low Likelihood) then early steps along the chain are discarded as 'burn-in'. The number of models discarded is usually decided to be once the Likelihood reaches some stabilized level, or when models provide a satisfactory fit to data given estimated noise levels. In addition, the chained is 'thinned' in order to reduce the correlation of nearby samples along the chain. In this procedure, only every n^{th} model is taken into account. The collected output samples from all chains after burn-in and thinning is referred to as the 'ensemble'. Statistical properties of this ensemble, such as mean and standard deviation, can then be calculated to aid the interpretation of the results.

In this study, we use a recently developed extension in which the model space is defined by a network of spherical Voronoi cells forming an irregular mesh over the 2D sphere (Pejić et al., 2019; Burdick et al., 2019). Spherical Voronoi cells directly partition a spherical surface, which is critical for global tomographic studies. We view this as an improvement over previously employed Cartesian Voronoi cells parameterizations (e.g. Young et al, 2013, Tkalčić et al., 2015) defined through a Cartesian projection over the sphere. The implementation of spherical Voronoi cells removes

distortion at the poles inherent with the Cartesian approach, and also naturally accommodates cyclicity over the globe.

4. Resolution tests

We carried out two all-inclusive synthetic tests (Fig. 4), two synthetic tests with simpler shapes and a synthetic test including a model with smooth variations (Supporting Information, Fig. S4) to assess the resolving power of our ray coverage (Fig. 2) and the capabilities of the HTDBI method. We used the data predicted by the two models featured in Fig. 4 and added Gaussian noise with the standard deviation of σ_N=0.5 s to the travel times. Velocity perturbations, relative to an average PREM velocity in the lowermost 300 km of the mantle, were allowed to range in the interval ±4%.

Our synthetic tests are improvements over the checkerboard pattern tests as they check the recovery of coexisting heterogeneities of different sizes and shapes. They examine retrieval of both simple and more complex heterogeneous structures with sharp boundaries as well as varying strengths in S-wave speed in D''. The first synthetic test (Fig. 4a) examines recovery of a pseudo, complex heterogeneity in D'' dominated by the spherical degree 2 anomalies (LLSVPs) as revealed in numerous long-period S-wave tomographic studies, but assumes other, smaller-scale features of varying amplitudes superimposed on the main signature. For example, it includes fast and slow velocities outside of the LLSVPs, beneath Central America, Alaska, Greenland, East Asia, South-East Asia and Australia.

The second synthetic test (Fig. 4b&c) includes the maximum power amplitudes and explores the recovery of several multi-scale features of different shapes (circle, rhombus, square and a small circle) that are superimposed on top of a predominantly hemispherical structure with sharp boundaries (Young et al., 2013; Tkalčić et al., 2015). The size of the overlaying anomalies onto the hemispherical structures varies from 5000 km (the diameter of the big circles) to 300 km (the narrow parts of the squares). We show the mean and standard deviation of the posterior ensemble in the second and third row of Fig. 4, respectively. The recovery of both long- and short-scale features in the synthetic tests highlights the benefits of the HTDBI approach. As expected, the best model-recovery is achieved in regions with a dense ray coverage, in particular North Africa, North Atlantic, Asia, and Australia.

In our synthetic tests, we used 6 Markov chains with 3 million iterations in each chain. The first 200,000 iterations were discarded as burn-in period and every 250th model was selected during the thinning procedure. We let the number of cells vary from 50 to 2000. Since the number of the model parameters can change, the required number of cells to fit the data can be expressed as a posterior probability distribution function. The histograms for the number of cells for both synthetic tests are shown in Fig. 5. In these synthetic examples, the true noise is known and there is no need to use

hierarchical sampling to estimate the character and level of the noise. However, adding the noise as a free parameter gives us confidence that we are able to recover noisy data in the inversion (Bodin et al., 2012). Therefore, as in a hierarchical approach, we allowed the scaling factor, λ, to be estimated through the inversion in all of our synthetic tests. As we added Gaussian random noise to the synthetic travel times and introduced the same value for σ with a standard deviation of 0.5, we expect λ to arrive at a value around 1 (equation 3). The histogram of λ (Fig. 5b & 5d) confirms that the data noise is properly resolved.

From synthetic test #1, it is evident that the method is able to retrieve the pattern and strength of the model parameters with a good resolution in areas with reasonable ray coverage. The ensemble mean of the retrieved models from inversion of the synthetic travel times illustrates that the combination of our ray coverage and this inversion scheme is successful in recovering both long- and short-scale features. According to the synthetic tests, small and large structures are well resolved at most parts of the northern hemisphere and Australia. We should expect smearing and distortions to happen in the east Pacific and parts of the southern hemisphere which is also evident in the standard deviation maps (Fig. 4g, 4h & 4i), and this is in agreement with the ray coverage (Fig. 2). The higher standard deviation occurs in the poorly sampled regions and at the sharp boundaries of positive and negative anomalies, which has been shown to be associated with uncertainty in boundary locations (Hawkins et al., 2019). The northern hemisphere is characterized by a higher ray coverage which results in a lower standard deviation and a good capacity to recover the details of S-wave speed variations. In contrast, the poorly sampled areas or the sharp velocity transitions go through more versatility in parameterization (mobile geometry of the Voronoi cells) and hence have a higher standard deviation.

5. Inversion

We used our high-quality, hand-picked measurements collected through waveform correlation, corrected the differential travel times for the effect of mantle structure and simulated the shear wave structure in the D''. In the HTDBI approach often a number of chains are utilized to thoroughly sample the model space. Here, at each chain, the initial 200,000 burn-in iterations were discarded and every 250^{th} model was selected for further processing (similar to the synthetic tests). Note that these chains start at a different random point and sample the model space independently. We allowed between 50 and 2000 cells with a uniform prior PDF over the globe, and set the shear wave velocity perturbation with a uniform prior in the interval <-7.5, 5%> relative to an average PREM shear-wave speed in D''. A uniform prior PDF for the model parameters means that the possible outcome could be with equal probability within the prior bound but not outside. The hierarchical parameter, λ, was

set over the range <1.0e-9, 1.0e1> and is sampled from the Jeffreys prior distribution. Bounds of the priors are set to include all possible values that a model parameter can take.

The determining factors for the resulting number of Voronoi cells and their spatial distribution are the ray distribution and the noise amplitude. Larger Voronoi cells form in the regions of scattered sampling while much smaller ones form in the regions of denser sampling (Bodin and Sambridge, 2009). We performed the inversion hierarchically, meaning that the noise is treated as a free parameter in the inversion (i.e. the inversion attempts to explore the trade-off between the model complexity (the number of Voronoi cells) and the observational noise (hierarchical error)).

Our LM-HTDBI approach generates a total of 54 million models. Given our burn-in period and the thinning stage, the posterior inference ends up with an ensemble of 180,000 models. Each model of the ensemble is a crude and implausible representation of the D'', however, the mean of many such crude models represents a more interpretable field of shear-wave velocity variation in D''.

6. Results

The mean and standard deviation of the posterior ensemble solution can be expressed visually by plotting them on a pixeled 2-D velocity map. To suppress the effect of the mantle on our differential travel times, we have tested a number of mantle models and analyzed the corresponding corrections for 3-D mantle structure. The structure of the mantle has been imaged by different research groups and some differences can be observed among them, which makes the decision of choosing a mantle model non-trivial. Here we have taken a more general approach, explained below.

6.1 Mantle correction

Given the variability among global mantle models and to avoid possible bias towards a specific one, we corrected our differential travel times using five different mantle models including TX2011 (Grand, 2002), GyPSuM (Simmons et al., 2010), SAW642ANb (Panning et al., 2010), S362ani+M (Moulik & Ekström 2014) and SEMUCB-WM1 (French & Romanowicz 2014). We ran nine Markov chains for each corrected dataset, resulting in 45 chains with 1.2 million model-iterations performed under each chain. The resulting D'' models inferred from data corrected for these five models are presented in Fig. 6. The patchy distribution of high- and low- velocity structure is independent of our choice of mantle model and shows more or less a consistent image of D'' (Fig. 6a to 6e). The short-scale heterogeneities exist across all five models obtained from corrected data sets, which suggests

353 that these patchy anomalies are a feature of the Earth's structure at D'' rather than a bias towards a
354 specific mantle model.

355 We show the chain history of negative log-likelihood as a function of iterations for 45 Markov chains
356 in Fig. 7. The chain history of negative log-likelihood demonstrates that all Markov chains stabilize
357 around a similar value (left panel in Fig. 7). A significant overlap can be observed in the histograms
358 of different chains, which demonstrates that all chains converged to a similar set of models (right
359 panel in Fig. 7).

360 Posterior probability plots of the data noise and the number of cells show the estimated noise in the
361 dataset and the number of Voronoi cells to which the inversion converges (Fig. 8a & 8b). The
362 frequency histogram of the number of cells shows a Gaussian distribution with a maximum centered
363 on 600 cells. Fig. 8c shows three distinctive groups representing the trans-D ensembles recovered
364 from the five different data corrections used. They are not due to different chains converging to
365 different parts of the model space. Hence in this figure, we see the effect of the change in data on the
366 ensemble. The key things to note are that the effect of the change in model correction on the
367 distribution of cell numbers is not significant since all are centered around 600-650 cells, and most
368 have similar spreads. The hierarchical noise parameter, λ, sees the most change, which again is
369 understandable since each correction results in different levels of scatter in the observations and
370 hence differing levels of data consistency (or noise). A sampling of the λ parameter responds
371 precisely to this effect. It will be higher when the (uncorrelated) residual scatter is larger and smaller
372 otherwise. Also, the slope of each cluster in terms of the λ vs. the number of cells is also as expected,
373 i.e., when λ becomes larger (data noise is assumed larger), then fewer numbers of cells tend to be
374 introduced, and vice versa. The Natural Parsimony principle can be seen in action on the distribution
375 of cells as fewer models with a higher number of cells are sampled. The natural parsimony is also
376 evident in Fig. 8c, since there is a negative correlation between data noise level and numbers of cells
377 introduced by the algorithm. This is consistent with the fact that more cells, and hence structure, are
378 required when there is more apparent signal in the data (noise levels are lower). Given that the
379 majority of the models recovered in the inversion have around 600 cells, this signifies a well-
380 sampled parameter space. Also, given that the inversion was performed with data noise as a free
381 parameter, we show the frequency histogram for the scaling factor of the hierarchical parameter, λ.
382 Since we assumed a $\sigma = 5\%$, and given the peak value of 0.27 in the distribution of λ, the estimated
383 noise in HTDBI is about 1.35% (σ_N, in equation 3). Given this estimation for data noise, and

assuming a typical travel time of 170 seconds for ScS within D'', we arrive at a representative traveltime uncertainty of about 2.3 s for our dataset.

6.2 Shear-wave velocity in D''

We combine the models with different mantle corrections (Fig. 6a-e) to obtain the mean and standard deviation over all models with the assumption that they all have equal weight. Therefore, our S-wave velocity variations in the D'' is the average of five models. This average velocity model and its associated standard deviation map are shown in Fig. 9. We compare the travel-time residual of the mean model (Fig. 9 a) with an individual Voronoi-cell model (Supporting Information, Fig. S5) and the initial travel-time residuals in the Supporting Information, Fig. S6. The histogram shows that the mean of the posterior ensembles can reduce travel time residuals compared to a single Voronoi-cell model shown in (Fig. S5) and the average velocity in PREM.

Following Simons et al (2006), we filtered the tomographic image of this study along with other tomographic models: SGLOBE-rani (Chang et al., 2015), S362ANI+M (Moulik and Ekström, 2014), SP12RTS (Koelemeijer et al., 2016), GyPSuM (Simmons et al., 2010), S40RTS (Ritsema et al. 2011), SEMUCB-WM1 (French & Romanowicz, 2014) and HMSL (Houser et al., 2008) to the low spherical harmonic degree, lmax=6 (Fig. 10). The long-scale patterns in LM-HTDBI are in general agreement about low velocities beneath Africa and the Pacific and fast in most parts of Asia and Antarctica. However, there is a striking difference across the existing global models, even for long-scale features in the shape and intensity of the LLSVPs (Fig. 10). The critical characteristic of our tomographic model is the appearance of short-scale features at the base of the mantle exterior to the LLSVPs, which our resolution analysis confirms are not artifacts of the inversion. In the Supporting Information (Fig. S7), we examine the heterogeneity-spectrum or the power-spectrum of the models. Spectral analyses reveal the long-scale content of our model is similar to the previous models as shown in the filtered plots (Supporting Information, Fig.10 and Fig. S7); however, its power of heterogeneity in higher degrees is larger than previous estimates (Fig. S7).

The main advantage of our approach over previous approaches is that as no explicit subjective regularization or parameterization are applied, the size of velocity heterogeneities is directly controlled by the data itself and the short-scale features are preserved. In terms of a comparison with other lowermost mantle models, we confirm that our model correlates well with SEMUCB-WM1 in terms of short-scale heterogeneity content, but it has more intense variation in velocity in comparison with the latter. The areas with the lowest and the highest shear-wave speed are scattered throughout

the lowermost mantle. Four specific examples of regions with high-velocity are mid-Indian ocean, west Australia, North Atlantic and North Chile. From Fig. 8b, it is obvious that the areas with higher standard deviation correspond to either the poorly sampled parts of D'' or to the areas that have gone through more velocity variations during the inversion (e.g. closer to the sharp contrasts in elastic properties).

7. Discussions

The chief goal of this study was to invert for the shear-wave velocity heterogeneities atop the CMB using ScS and S travel times. Our study has a couple of limitations. The first limitation is that we assume a fixed thickness of 300 km for the D'' layer. In addition, our forward method does not include the finite frequency effects. However, ray-theory based tomography at the frequencies we use is a reasonable approximation to interpret finite frequency travel times. For example, Hung et al. (2005) and Castle et al. (2000) used ScS-S data at the periods of 20 s to perform inversions with and without the sensitivity kernels. They showed that the tomography based on the sensitivity kernels yields similar results using infinite frequency ray paths. Hung et al. (2005) showed that the recovered velocity perturbations using finite frequency kernels (in the frequency band similar to our data) are approximately 1–2 times larger than those from the ray-based kernels. In our study, given the average number of 600 Voronoi cells for the area covering the CMB (Fig. 8a), the average diameter of a simplified Voronoi cell is ~ 500 km, which is slightly larger than the diameter of the Fresnel zone (400 km). The structures we interpret are also larger than the size of the Fresnel zone. Hence, not accounting for finite frequency effects might not be a too severe limitation.

Another limitation of our approach is that the inversion scheme we deploy does not assess an independent impact of anisotropy on S and ScS data, and in turn, on our tomograms. Within the Bayesian framework, not accounting for anisotropy is considered a theory error. Accounting for both data noise and theory errors is at the leading edge of geophysical inference studies. Accurate mapping seismic anisotropy in the lowermost mantle using tomographic methods is challenging and still an open question (Romanowicz & Wenk, 2017). Many studies used differential measurements of pair phases such as ScS and S to calculate anisotropy in D'' (e.g., Wookey et al., 2005a; Nowacki et al., 2010; Lay, 2015). Shear wave splitting measurements of D'' show that horizontally polarized S-wave velocities are larger than vertically polarized ones by ~1% (Panning & Romanowicz, 2004). The residual splitting in ScS, which is attributed to the anisotropy of D'' shows lag times between 1.0 and 3.9 s for epicentral distances 60◦ to 85◦ beneath the north Pacific (Wookey et al., 2005).

Our tomographic approach in a combination with a high-quality dataset enables a multi-scale imaging of the lowermost mantle. Our model (LM-HTDBI) reveals multi-scale structures ranging in wavelengths from hundreds to thousands of kilometers. The deduced shear-wave tomogram of D'' also reveals that the amplitudes of the short-scale low-velocity anomalies outside the LLSVPs are comparable to those observed inside them. Also, the morphology of the LLSVPs imaged by our method features small high-velocity patches creating separate regions of low-velocity anomalies, rather than only two large, unified and smooth LLSVPs. In addition, the appearance of the short-scale structures distorts the general shape of the LLSVPs as their margins do not look uniformly flat.

The results of this study are in general agreement with the D'' P-wave tomography of Tkalčić et al. (2015) using the HTDBI method in that both models contain short-scale and medium-scale structures superimposed on top of the long-scale structures. Furthermore, Muir and Tkalčić (2020) have recently obtained a similar result using Hamiltonian Monte Carlo sampling and low-degree spherical harmonics expansion with implicit regularization by basis truncation. They showed that short-scale perturbations are required to account for the observed travel-time residuals.

The complex pattern of short-scale heterogeneities that we obtained suggests that LLSVPs are not necessarily the only contributing factors to mantle instabilities. Given the existence of short-scale heterogeneities, we believe that it is feasible that they play a significant role in mantle dynamics. Several regional studies found evidence for locally sharp variation (up to or more than ±4%) in regions like eastern Eurasia (He & Wen, 2011), western Pacific (e.g. He et al., 2006; Takeuchi 2012; Suzuki et al., 2020) and the Caribbean (Hung et al., 2005). The recent study of Suzuki et al., (2020) illustrated several strong short-scale, low shear-wave velocities in the western Pacific and northern Australia. For instance, in ULVZs, shear-wave velocity reduction can reach 30 – 45% (e.g. Cottaar & Romanowicz 2012; Yu and Garnero 2018; Jenkins et al., 2021) and many of them show complex internal radial structures (Pachhai et al., 2014; 2015). We cannot expect to reveal such a level of details in our tomograms as the thickness of ULVZs varies most likely between 5 and 10 km (Garnero et al., 2016) or on the order of 20 – 30 km in the case of the Hawaiian mega-ULVZ (Cottaar and Romanowicz 2012; Jenkins et al., 2021). Our model presents an averaged image of D'' with approximately 300 km thickness. Hence, some theory limitations inevitably contribute to the noise and are captured by our estimates of observational uncertainty through the hierarchical noise estimation. A recent study by Kim et al. (2020) found evidence of pervasive scattering (Sdiff postcursors present on ~50% of paths) across the Pacific without a clear relationship between the postcursors' amplitudes and delay-times, suggesting either distributed heterogeneities or interaction

with boundaries of a larger structure. We speculate that the significant amplitude Vs variation obtained in this study is probably significant enough to produce the postcursors detected by Kim et al. (2020).

Our study reveals short-scale heterogeneities on top of the long-scale structures while most global models imaged predominantly long-scale features in D''. The method adopted here alleviates some of the shortcomings of using classical inversion methods including block parameterization, smoothing and damping regularization. Importantly, inverting independently for ScS-S and correcting for the mantle heterogeneities enables us to isolate the lowermost mantle from the heterogeneities in the rest of the mantle. To further investigate these differences, we compared seven different global maps of shear wave variations at D'' including SGLOBE-rani (Chang et al., 2015), S362ANI+M (Moulik and Ekström 2014), SP12RTS (Koelemeijer et al. 2016), GyPSuM (Simmons et al., 2010), TX2011 (Grand 2002), SEMUCB-WM1 (French & Romanowicz 2014) and HMSL (Houser et al., 2008) with our model (Fig. 11). More broadly, these models were derived either from different datasets or by using different methods of inversion.

Fig. 10 and Fig. 11 reveal that there are similarities among different models for long-scale features: they agree on the existence and extent of large low-velocity patterns, the well-known LLSVPs, under the Pacific and Africa. However, the margins, shapes, strength of heterogeneity and gradients across the D'' are significantly different. Although the data coverage is usually better in the northern hemisphere, most of the models in D'' do not capture small-scale heterogeneities, which we speculate is most likely due to applying uniform damping and smoothing. For example, an interesting observation from our comparison with other global models (Fig. 11) is a clear difference in the recovery of short-scale anomalies between the HMSL model and this study. We employed a subset of data used in the HMSL model, which only includes data from larger epicentral distances. Although the outline of the LLSVPs is similar, the presence and lack of short-scale features represent a striking difference between these two models. This is attributable to the inversion strategy deployed here where no fixed model parameterization, damping and smoothing are required, and noise is treated as a free parameter, which is achieved at a significantly higher computational cost.

Another clear difference among the models selected for comparison is the amplitudes of Vs variations. This is not surprising as different modelers use different data and methods, and they achieve different resolutions in different regions. We compared the amplitudes of LM-HTDBI with the previous models in the Supporting Information (Fig. S8), as in Burdick & Lekić (2017). The tilt of the ellipses in Fig. S8 shows that velocity variations in our model have higher amplitude relative

to the previous studies. Among all models presented in Fig. 11, SEMUCB-WM1 is generally consistent with our model in places where they both exhibit larger amplitudes of S-wave velocity heterogeneity, as well as in the features not seen in earlier generations of global D'' models. However, these two models certainly differ in detail, especially in terms of the location and distribution of short-scale heterogeneities. The existence of some short-scale features in SEMUCB-WM1 is likely due to the usage of short-period waveform data.

The only low-velocity anomaly outside of the LLSVPs that emerges in the majority of global models is the 'Perm anomaly' (e.g. Lekić et al., 2012), north of the Caspian Sea. The region around Perm anomaly is imaged as two smaller low-velocity anomalies in our model and this region is well constrained in our synthetic test (Fig. 4 d).

A possible origin and composition of the LLSVPs presented in global tomographic images of D'' is still enigmatic (e.g., Garnero et al., 2016; Doucet et al., 2020), yet our tomographic model confirms a significantly more complex image of D''. The base of the mantle outside of the LLSVPs has long been considered as the site of accumulation of cold subducted slabs (Grand, 2002; Jones et al., 2020; Suzuki et al., 2020; Li 2020). This is a possible explanation for the existence of high shear-wave velocity regions. A recent study by Li (2020) showed that the scattered low-velocity anomalies outside of the LLSVPs could have a hot thermal origin that are detached from the thermochemical piles. Along the same line, the existence of fast seismic velocity anomalies within LLSVPs might suggest principally thermal-heterogeneity characterized by the clusters of plumes (Davies et al., 2015; Tkalčić et al., 2015, Muir & Tkalčić, 2020, Davaille & Romanowicz 2020).

8. Conclusions

This study presents a new model of shear-velocity variations in the D'' using high quality, handpicked dataset of S and ScS differential travel times through waveform correlation. Inverting for the compilation of 18,131 ScS-S differential travel times in conjunction with careful consideration of global mantle models enabled us to "isolate" the lowermost mantle from the heterogeneities present in the rest of the mantle. In this paper, we assumed that the D'' could be modeled as a single layer. We utilized recent improvements in the inversion technique through the use of the HTDBI framework which is based on implicit parametrization (spherical Voronoi cells) and treats the model complexity and the data noise as free parameters, while a uniform application of damping and smoothing to the model space can be avoided. We found that our model is in agreement with most of

the recent global studies in terms of imaging the long-scale features at the base of the mantle. However, short-scale heterogeneity, as seen in our D'' tomogram, is far more omnipresent than in spherical-harmonic, degree-2-dominated images for shear-wave speed of the lowermost mantle obtained in most global models. This is the most striking difference between our model and the previous model obtained using the same subset of data (Houser et al., 2008). We demonstrate, however, that our method is able to recover much simpler, degree-2 images of the lowermost mantle if the lowermost mantle is indeed void of short- and medium-scale heterogeneity and only characterized by long-scale features. We are thus confident that the tomogram of the lowermost mantle we obtain is a realistic representation of the seismic structures. Significantly, the recovered LLSVP morphology of is complex, consisting of smaller high-velocity patches among low-velocity domains. The newly obtained image suggests that the LLSVPs' margins are not uniformly flat. We further argue that the methodology we adopt is a significant step forward in imaging the complicated structure of the D'' layer on a global scale, and provides an important bridge between long-scale features at a global scale and short-scale features of regional models. Future work may explore combining additional datasets of travel times to increase spatial coverage and resolution of the lowermost mantle, adopting similar principles in full-waveform modeling and novel methodological approaches to inversion.

Acknowledgment

We thank Guy Masters for sharing his dataset with us, and his insights into the interpretation of our results. The authors would like to thank the associate editor Ved Lekić, Ed Garnero, and an anonymous reviewer for constructive discussions and feedback. We used GMT (Wessel et al., 1998) to plot the figures. We downloaded the data from IRIS DMC via the Wilber 3 tool (http://ds.iris.edu/wilber3). Calculations were performed on the Terrawulf cluster, a computational facility supported through the AuScope Ltd. AuScope is funded under the National Collaborative Research Infrastructure Strategy (NCRIS), and the Education Investment Fund (EIF3) both Australian Commonwealth Government Programs. Numerical simulations were undertaken on the NCI National Facility in Canberra, Australia, which is supported by the Australian Commonwealth Government. Generic Trans-dimensional Voronoi Cell Code for surface spherical problems is available through https://zenodo.org/record/4771010#.YKRI7Kgzabg.

577 **Figure Captions**

578

579 ***Fig. 1.*** a) Diagram of S and ScS raypaths from hypocenter (star) to receivers (reversed triangles) at
580 epicentral distances of 45° and 75°. b) Histogram of data distribution (40,843 rays) based on
581 epicentral distances (Houser et al., 2008). The red dashed line indicates the portion of data (16,144
582 rays) that was selected for this study.

583

584 ***Fig. 2.*** The D" sampling by the ray coverage in this study. The green rays are a subsample of
585 Houser et al., (2008) for epicentral distances of 60-75 deg. The blue rays are the newly-picked data
586 which include events from 2008 to 2018 (1,787 rays). b) Distribution of ScS bounce points of the
587 newly picked dataset on the CMB. Observed ScS-S travel time residuals relative to PREM projected
588 at the bouncing points of ScS. c) Distribution of ScS bounce points of Houser et al., (2008) on the
589 CMB. The gray lines beneath the bouncing points represent ray path at D''.

590

591 ***Fig. 3.*** An example of S and ScS alignment to measure the differential travel time of S and ScS for
592 two events 2017-02-24T17:28:44 and 2008-02-25T21:02:19 recorded at stations GIRL, BEAR and
593 CMSA. The measurement technique is manual fitting of the S and ScS waveforms concentrating on
594 the first half cycle. The y-axis is normalized to the maximum amplitude.

595

596 ***Fig. 4.*** Two synthetic tests designed to show the resolving power of ScS in the lowermost mantle
597 based on the ray coverage shown in Fig. 1. Top row is the input models, second one is the recovered
598 mean model and third row is the estimated standard deviation. a) The synthetic test that mimics the
599 D'' pattern obtained in most studies. b) A hemispherical multi-scale synthetic test centered at 0^o. c)
600 Same as b) but centered at 180^o. The positive anomalies are 4% faster than the PREM average
601 velocity and the negative anomalies are 4% slower. d), e) and f) are the recovered mean models. g),
602 h) and i) are the standard deviation of the posterior ensemble.

603

604 ***Fig. 5.*** The posterior probability distributions of the number of cells and the hierarchical parameter:
605 a) and b) for the synthetic test #1. c) and d) for the synthetic test #2.

606

607 ***Fig. 6.*** S-wave velocity perturbations from the PREM of D'' using mantle corrections according to
608 the following models: a) TX2011 (Grand, 2002), b) SEMUCB-WM1 (French and Romanowicz,
609 2014), c) GyPSuM (Simmons et al., 2010), d) SAW642ANb (Panning et al., 2010) and e)
610 S362ANI+M (Moulik and Ekström, 2014).

Fig. 7. Chain history of 45 chains from five models each including 9 chains that presented in Fig. 6. Each color line represents a chain. The vertical axis is Negative-log likelihood from equation 2, and the iterations are shown in the horizontal axis. The right panel shows the histograms of the Negative-log likelihood functions across the chains. The overlapping histograms indicates that all the chains converged to a similar set of models and different corrections lead to chains with similar likelihoods.

Fig. 8. a) Posterior probability distributions of the number of Voronoi cells used to describe LM-HTDBI. b) Posterior probability distributions of the hierarchical parameter, λ, of the data noise. c) Distribution of hierarchical parameter (estimated noise in the data) versus numbers of cells. Each color represents a different chain. The trade-off is, as expected, where higher data noise (λ) results in fewer unknowns, and hence less structure is introduced. This property is often termed 'natural parsimony'.

Fig. 9. The average shear-wave velocity model of D'' (LM-HTDBI) calculated by averaging over the five models presented in Fig. 6. a) S-wave velocity perturbations from the PREM model and b) the corresponding standard deviation. This average model and standard deviation is determined across multiple McMC chains in Fig. 6, using the individual means and standard deviations in S-wave speed of each chain. By using some standard algebraic results this becomes equivalent to an equally weighted combination of the ensemble of models from all chains and all cases in Fig.6.

Fig. 10. Global maps of shear wave velocity variations at the core-mantle boundary for the eight models including SGLOBE-rani (Chang et al., 2015), S362ANI+M (Moulik and Ekström, 2014), SP12RTS (Koelemeijer et al., 2016), GyPSuM (Simmons et al., 2010), TX2011 (Grand, 2002), SEMUCB-WM1 (French & Romanowicz, 2014), HMSL (Houser et al., 2008) and this study (LM-HTDBI) filtered to the spherical-harmonic degree lmax = 6. Each model extreme value annotated on the top left side of their map. All scale bars are in %δVs and set to the ±5% to show the amplitude diversity between models.

Fig. 11. Comparison of the global shear-wave velocity models for the lowermost mantle. All scale bars are in %δVs and set to the ±5% to show the amplitude diversity between models. The tomographic models for eight models shown in Fig. 10. As in Fig. 10, the numbers in the corner of each panel show maximum variation for each filtered model and scale bars are set to ±5%.

645

References:

Avants, M., Lay, T., & Garnero, E.J. (2006). A new probe of ULVZ S-wave velocity structure: Array stacking of ScS waveforms. *Geophys. Res. Lett*., 33, L07314. https://doi:10.1029/2005GL024989

Bréger, L., & Romanowicz, B. (1998). Three-dimensional structure at the base of the mantle beneath the central Pacific. *Science*, 282 (5389), 718–720.

Bodin, T., Sambridge, M., Rawlinson, N., & Arroucau, P. (2012). Trans-dimensional tomography with unknown data noise. *Geophys. J. Int*., 189, 1536–1556.

Bower, D. J., Gurnis, M., & Seton, M. (2013). Lower mantle structure from paleogeographically constrained dynamic Earth models. *Geochem. Geophys. Geosyst*., 14, 44–63.

Buland, R., & Chapman, C. (1983). The computation of seismic travel times. *Bull. Seismol. Soc. Am.*, 73(5).

Bull, A. L., McNamara, A. K., & Ritsema, J. (2009). Synthetic tomography of plume clusters and thermochemical piles. *Earth. Planet. Sci. Lett*., 278, 152–156. https://doi: 10.1016/j.epsl.2008.11.018

Burdick, S. & Lekić, V. (2017). Velocity variations and uncertainty from transdimensional *P*-wave tomography of North America, *Geophysical Journal International*, Volume 209, Issue 2, Pages 1337–1351, https://doi.org/10.1093/gji/ggx091

Burdick, S., Waszek, L., & Lekić, V. (2019). Seismic tomography of the uppermost inner core. *Earth. Planet. Sci. Lett.*, 528:115789.

Chang, S-J., Ferreira, A.M.G., Ritsema, J. van Heijst, H. J., & Woodhouse, J. H. (2015). Joint inversion for global isotropic and radially anisotropic mantle structure including crustal thickness perturbations. *J. Geophys. Res. Solid Earth*, 120, 4278–4300. https://doi:10.1002/2014JB011824

Christensen, U. R., & Hofmann, A. W. (1994). Segregation of subducted oceanic crust in the convecting mantle. *J. Geophys. Res*., 99, 19867.

Cottaar, S., Lekić, V. (2016). Morphology of seismically slow lower-mantle structures, *Geophysical Journal International*, Volume 207, Issue 2, Pages 1122–1136, https://doi.org/10.1093/gji/ggw324

Cottaar, S., & Romanowicz, B. (2012). An unusally large ULVZ at the base of the mantle near Hawaii. *Earth Planet. Sci. Lett.*, 355–56, 213-222. https://doi.org/10.1016/j.epsl.2012.09.005.

Creasy, N., M. D. Long, and H. A. Ford (2017), Deformation in the lowermost mantle beneath Australia from observations and models of seismic anisotropy, J. Geophys. Res. Solid Earth, 122, 5243–5267, doi:10.1002/ 2016JB013901.

Davaille, A., & Romanowicz, B. (2020). Deflating the LLSVPs: Bundles of mantle thermochemical plumes rather than thick stagnant "piles". Tectonics, 39, e2020TC006265. https:// doi.org/10.1029/2020TC006265

Davies, D. R., Goes, S. & Lau, H. C. P. (2015). Thermally-dominated deep mantle LLSVPs: A review. The Earth's heterogeneous mantle, Editors: A. Khan & F. Deschamps, Springer Geophysics, https://doi: 10.1007.978-3-319-15627-9_14.

De Andrade, E. S., & Liu, Q. (2017). Fast computation of global sensitivity kernel database based on spectral-element simulations. Pure and Applied Geophysics, 174(7), 2733-2761. - see ScS kernel calculations on accompanying website: https://www8.physics.utoronto.ca/~liuqy/SEM_kernels/

Dobson, D., & Brodholt, J. (2005). Subducted banded iron formations as a source of ultralow-velocity zones at the core–mantle boundary. *Nature*, 434**,** 371–374. https://doi.org/10.1038/nature03430

Doucet, L.S., Li, Z.X., Ernst, R.E., Kirscher, U., Gamal El Dien, H., & Mitchell, R.N. (2020). Coupled supercontinent-mantle plume events evidenced by oceanic plume record. Geology 48 (2), 159–163. https://doi.org/10.1130/G46754.1.

Durand S., Debayle, E., Ricard, Y., Zaroli, C. & Lambotte, S. (2017). Confirmation of a change in the global shear velocity pattern at around 1,000 km depth, *Geophys. J. Int*., 211(3), 1628-1639.

French, S. W., & Romanowicz, B. (2014). Whole-mantle radially anisotropic shear-velocity structure from spectral-element waveform tomography, *Geophys. J. Int*., 199, 1303–1327.

Frost, D.A., Rost, S., Selby, N.D., & Stuart, G.W. (2013). Detection of a tall ridge at the core-mantle boundary from scattered PKP energy. *Geophys. J. Int*., (ISSN 0956-540X) 195 (1), 558–574.

Fukao, Y., Widiyantoro, S., & Obayashi, M. (2001). Stagnant slabs in the upper and lower mantle transition region. *Rev. Geophys*., 39, 291-323.

Garnero, E.J., & Helmberger, D.V. (1995). A very slow basal layer underlying large-scale low velocity anomalies in the lower mantle beneath the Pacific: evidence from core phases. *Phys. Earth Planet. Int*., 91, 161-176.

Garnero, E., & McNamara, A. (2008). Structure and dynamics of Earth's lower mantle. *Science*, 320(5876), 626–628.

Garnero, E. J., McNamara, A. K., & Shim, S.-H. (2016). Continent-sized anomalous zones with low seismic velocity at the base of Earth's mantle. *Nat. Geosci.*, 9, 481–489.

Geyer, C.J. & Møller, J. (1994). Simulation procedures and likelihood inference for spatial point processes. Scandinavian Journal of Statistics, 21, 359–373.

Grand, S. P. (2002). Mantle shear wave tomography and the fate of subducted slabs. *Phil. Trans. R. Soc. Lond. A* 360, 2475-2491.

Garcia, R., S. Chevrot, and M. Calvet (2009), Statistical study of seis- mic heterogeneities at the base of the mantle from PKP differential traveltimes, *Geophys. J. Int*., 179, 1607–1616.

Green, P.J. (1995). Reversible jump Markov chain Monte Carlo computation and Bayesian model determination, Biometrika, 82, 711–32.

716 Hawkins, R. (2021). rhyshawkins/GeneralVoronoiS2: Mousavi et al release (Version 1.0.0). Zenodo.
717 http://doi.org/10.5281/zenodo.4771010

718 Hawkins, R., Bodin, T., Sambridge, M., Choblet, G., & Husson, L. (2019). Trans-dimensional
719 surface reconstruction with different classes of parameterization. Geochemistry, Geophysics,
720 Geosystems, 20, 505–529. https://doi.org/10.1029/2018GC008022

721 Hosseini, K., Sigloch, K., Tsekhmistrenko, M., Zaheri, A., Nissen-Meyer, T., & Igel, H. (2020). Global
722 mantle structure from multifrequency tomography using *P*, *PP* and *P*-diffracted waves, *Geophys. J. Int.*,
723 220(1), 96–141. https://doi.org/10.1093/gji/ggz394

724 Houser, C., Masters, G., Shearer, P., & Laske, G. (2008). Shear and compressional velocity models
725 of the mantle from cluster analysis of long-period waveforms. *Geophys. J. Int.*, 174, 195–212.

726 He, Y., & Wen, L. (2009), Structural features and shear-velocity structure of the "Pacific Anomaly".
727 *J. Geophys. Res*., 114, B02309. https://doi:10.1029/2008JB005814.

728 He, Y., & Wen, L. (2011). Seismic velocity structures and detailed features of the D″ discontinuity
729 near the core-mantle boundary beneath eastern Eurasia, *Phys. Earth Planet. Int.*, 189, 176–184.

730 Hung, S.-H., Garnero, E.J., Chiao, L.-Y., Kuo, B.-Y., & Lay, T. (2005). Finite-frequency
731 tomography of D'' shear velocity heterogeneity beneath the Caribbean. *J. Geophys. Res.*, 110,
732 B07305. https://doi: 10.1029/2004JB003373

733 Ishii, M., & Tromp, J. (1999). Normal-mode and free-air gravity constraints on lateral variations in
734 velocity and density of Earth's mantle. *Science*, 285, 1231–1236.

735 Jenkins, J., Mousavi, S., Li, Z. & Cottaar, S. (2021) A high-resolution map of Hawaiian ULVZ
736 morphology from ScS phases, Earth and Planetary Science Letters, Volume 563, 116885,ISSN 0012-
737 821X, https://doi.org/10.1016/j.epsl.2021.116885.

738 Jones, T. D., Maguire, R.R., van Keken, P.E., Ritsema, P.E., & Koelemeijer, P. (2020). Subducted
739 oceanic crust as the origin of seismically slow lower-mantle structures. *Progress in Earth and*
740 *Planetary Science*, 7, 17. https://doi.org/10.1186/s40645-020-00327-1.

741 Kim, D., Lekić, V., Menard, B., Baron, D. and Taghizadeh-Popp, M. (2020). Sequencing
742 seismograms: A panoptic view of scattering in the core-mantle boundary region. Science, 368(6496),
743 pp.1223-1228.

744 Koelemeijer, P., Deuss, A., & Ritsema, J. (2017). Density structure of Earth's lowermost mantle
745 from Stoneley mode splitting observations. *Nature Communications*, 8, 1–10.
746 https://doi.org/10.1038/ncomms15241

747 Kuo, C., & Romanowicz, B. (2002). On the resolution of density anomalies in the Earth's mantle
748 using spectral fitting of normal-mode data. *Geophys. J. Int*., 150, 162–179.

749 Kustowski, B., Ekstrom, G., & Dziewonski, A.M. (2008). Anisotropic shear-wave velocity structure
750 of the Earth's mantle: a global model. *J. Geophys. Res*., 113, B06306.

Labrosse, S., Hernlund, J. W., & Coltice, N. (2007). A crystallizing dense magma ocean at the base of the Earth's mantle. *Nature*., 450, 866–869.

Lau, H. C. P., Mitrovica, J. X, Davis, J. L., Tromp, J., Yang, H.-Y., & Al-Attar, D. (2017). Tidal tomography constrains Earth's deep-mantle buoyancy. *Nature*, 551, 321–326. https://doi.org/10.1038/nature24452.

Lekić, V., Cottaar, S., Dziewonski, A.M., & Romanowicz, B. (2012). Cluster analysis of global lower mantle tomography: A new class of structure and implications for chemical heterogeneity, *Earth Planet. Sci. Lett*., 357–358, 68–77.

Li, M., McNamara, A.K., Garnero, E.J., & Yu, S. (2017). Compositionally-distinct ultra-low velocity zones on Earth's core-mantle boundary. Nature Communications, 8(1), 177. https://doi.org/10.1038/s41467-017-00219-x

Li, M. 2020. The formation of hot thermal anomalies in cold subduction-influenced regions of Earth's lowermost mantle. J. Geophys. Res.: Solid Earth. https://doi.org/10. 1029/2019JB019312.

Li, Y., Miller, M.S., Tkalčić, H., Sambridge, M. (2021). Small-scale heterogeneity in the lowermost mantle beneath Alaska and northern Pacific revealed from shear-wave triplications, EPSL, Volume 559, 116768, ISSN 0012-821X, https://doi.org/10.1016/j.epsl.2021.116768.

Mackay, D. J. C. (2003). Information theory, inference, and learning algorithms. Cambridge, UK: Cambridge University Press

Masters, G., & Gubbins, D. (2003). On the resolution of density within the Earth. Physics of the Earth and Planetary Interiors, 140(1–3), 159–167. https://doi.org/10.1016/j.pepi.2003.07.008

Masters, G., Laske, G., Bolton, H. & Dziewonski, A. (2000) In Earth's Deep Interior: Mineral Physics and Tomography from the Atomic to the Global Scale, Geophysical Monograph Series 63–87 (eds Karato, S., Forte, A., Liebermann, R., Masters, G. & Stixrude, L.) (American Geophysical Union).

McNamara, A. K., & Zhong, S. (2005). Thermochemical structures beneath africa and the pacific ocean. Nature, 437(7062), 1136–1139. https://doi.org/10.1038/nature04066;10.1038/nature04066.

McNamara, A. K., Garnero, E. J., & Rost, S. (2010). Tracking deep mantle reservoirs with ultra-low velocity zones. Earth and Planetary Science Letters, 299, 1–9. https://doi.org/10.1016/j.epsl.2010.07.042.

McNamara, A. K. (2019). A review of large low shear velocity provinces and ultra low velocity zones. Tectonophysics, 760, 199–220. https:// doi.org/10.1016/j.tecto.2018.04.015

Moulik, P., & Ekström, G. (2014). An anisotropic shear velocity model of the Earth's mantle using normal modes, body waves, surface waves and long-period waveforms. Geophysical Journal International, 199(3), 1713–1738.

Muir, J.B., & Tkalčić, H. (2020). Probabilistic lowermost mantle P-wave tomography from hierarchical Hamiltonian Monte Carlo and model parametrization cross-validation, *Geophys. J. Int.*, 223, 1630-1643, https://doi.org/10.1093/gji/ggaa397

788 Mulyukova, E., Steinberger, B., Dabrowski, M., & Sobolev, S.V. (2015). Survival of llsvps for
789 billions of years in a vigorously convecting mantle: Replenishment and destruction of chemical
790 anomaly. Journal of Geophysical Research: Solid Earth, 120, 3824–3847. https://doi.
791 org/10.1002/2014JB011688

792 Nowacki, A., and Wookey, J. (2016). The limits of ray theory when measuring shear wave splitting
793 in the lowermost mantle with ScS waves. *Geophysical Journal International*, vol. 207, no. 3, pp.
794 1573-1583, doi: 10.1093/gji/ggw358.

795 Ni, S., & D.V. Helmberger (2001), Horizontal transition from fast to slow structures at the core-
796 mantle boundary; south Atlantic, Earth Planet. Sci. Lett., 187(3-4), 301–310..

797 Niu, F., Kelly, C., & Huang, J. (2012), Constraints on rigid zones and other distinct layers at the top
798 of the outer core using CMB underside reflected PKKP waves. Earthq Sci 25:17–24.

799 Pachhai, S., Tkalčić, H., & Dettmer, J. (2014). Bayesian inference for ultralow velocity zones in the
800 Earth's lowermost mantle: Complex ULVZ ´ beneath the east of the Philippines. Journal of
801 Geophysical Research: Solid Earth, 119, 8346–8365. https://doi.org/10.1002/2014JB011067

802 Pachhai, S., Dettmer, J., & Tkalčić, H. (2015). Ultra-low velocity zones beneath the Philippine and
803 Tasman Seas revealed by a transdimensional Bayesian waveform inversion. Geophysical Journal
804 International, 203(2), 1302–1318. https://doi.org/10.1093/gji/ggv368

805 Panning, M.P., V. Lekić, & Romanowicz, B. (2010), Importance of crustal corrections in the
806 development of a new global model of ´ radial anisotropy, J. Geophys. Res., 115, B12325,
807 doi:10.1029/2010JB007520

808 Pejić, T., Hawkins, R., Sambridge, M., & Tkalčić, H. (2019). Transdimensional Bayesian attenuation
809 tomography of the upperinnercore. Journal of Geophysical Research: Solid Earth, 124.
810 https://doi.org/10.1029/2018JB01640

811 Ricard, Y., Richards, M., & Le Stunff, Y.A. (1993). A geodynamical model of mantle density
812 heterogeneity. Journal of Geophysical Research, 98, 21,895–21,909.
813 https://doi.org/10.1029/93JB02216

814 Rost, S., & Earle, P.S. (2010), Identifying regions of strong scattering at the core-mantle boundary
815 from analysis of PKKP precursor energy, Earth Planet. Sci. Lett., 297, 616–626

816 Sambridge, M., T. Bodin, K. Gallagher, & Tkalčić, H. (2013), Transdimensional inference in the
817 geosciences, Philos. Trans. A. Math. Phys. Eng. Sci., 371(1984), 20,110,547

818 Simmons, N. A., Forte, A. M., Boschi, L., & Grand, S. P. (2010). GyPSuM: A joint tomographic
819 model of mantle density and seismic wave speeds. Journal of Geophysical Research, 115, B12310.
820 https://doi.org/10.1029/2010JB007631

821 Simons, F. J., Dahlen, F. A., & Wieczorek, M. A. (2006). Spatiospectral concentration on a sphere.
822 SIAM Review, 48(3), 504–536. https://doi.org/10.1137/S0036144504445765

823 Suzuki, Y., Kawai, K., Geller, R., Tanak, S., Siripunvaraporn, W., Boonchaisukc, S., Noisagool, S.,
824 Ishihara, Y., & Kim, T. (2020), High-resolution 3-D S-velocity structure in the D″ region at the

western margin of the Pacific LLSVP: Evidence for small-scale plumes and paleoslabs. Physics of the Earth and Planetary Interiors, 307, 106544. https://doi.org/10.1016/j.pepi.2020.106544

Tackley, P. J. (2012). Dynamics and evolution of the deep mantle resulting from thermal, chemical, phase and melting effects. Earth-Science Reviews, 110(1), 1–25. https://doi.org/10.1016/j.earscirev.2011.10.001

Takeuchi, N., Morita, Y., Xuyen, N. D., & Zung, N. Q. (2008). Extent of the low-velocity region in the lowermost mantle beneath the western Pacific detected by the Vietnamese broadband seismograph array. Geophysical Research Letters, 35, L05307. https://doi.org/10.1029/2008GL033197.

Takeuchi, N. (2012). Detection of ridge-like structures in the Pacific large low-shear-velocity province. Earth and Planetary Science Letters, 319–320, 55–4. https://doi.org/10.1016/j.epsl.2011.12.024

Tarantola, A. (2004). Inverse problem theory and methods for model parameter estimation. Philadelphia, PA: SIAM.

Tan, E., Gurnis, M., & Han, L. J. (2002). Slabs in the lower mantle and their modulation of plume formation. Geochemistry, Geophysics, Geosystems, 3(11), 1067. https://doi.org/10.1029/2001GC000238

Thomas, C., Weber, M., Wicks, C. W., & Scherbaum, F. (1999). Small scatterers in the lower mantle observed at German broadband arrays. Journal ofGeophysical Research: Solid Earth, 104(B7), 15073–15088. https://doi.org/10.1029/1999JB900128

Thorne, M.S., Garnero, E.J., Jahnke, G., Igel, H., McNamara, A.K. (2013). Mega ultra low velocity zone and mantle flow. Earth Planet. Sci. Lett. 364, 59–67

Tkalčić, H., & Romanowicz, B. (2002). Short scale heterogeneity in the lowermost mantle: insights from PcP-P and ScS-S data, *Earth Planet. Sci. Lett.* 201(1), 57-68, 2002.

Tkalčić, H., Young, M. K., Muir, J. B., Davies, R., & Mattesini, M. (2015). Strong, multi-scale heterogeneity in Earth's lowermost mantle, *Sci. Reports*, 5, 18416.

Trampert, J., Deschamps, F., Resovsky, J., & Yuen, D. (2004). Probabilistic tomography maps chemical heterogeneities throughout the lower mantle. Science, 306(5697), 853–856. https://doi.org/10.1126/science.1101996

Vidale, J. E., & Hedlin, M. A. H. (1998). Evidence for partial melt at the core-mantle boundary north of Tonga from the strong scattering of seismic waves. Nature, 391(6668), 682–685. https://doi.org/10.1038/35601

Young, M. K., Tkalčić, H., Bodin, T., & Sambridge, M. (2013). Global P wave tomography of Earth's lowermost mantle from partition modeling. *J. Geophys. Res.*, 118, 5467–5486. https://doi.org/10.1002/jgrb.50391

Yu, S., & Garnero, E. J. (2018). Ultra-low velocity zone locations: A global assessment. Geochemistry, Geophysics, Geosystems, 19, 396–414. https://doi. org/10.1002/2017GC007281

862 Wen, L., & Helmberger, D. V. (1998). Ultra low velocity zones near the core-mantle boundary from
863 broadband PKP precursors. Science, 279(5357), 1701–1703.
864 https://doi.org/10.1126/science.279.5357.1701

865 Wenk, H. R., Cottaar, S., Tomé, C. N., McNamara, A., & Romanowicz, B. (2011). Deformation in
866 the lowermost mantle: From polycrystal plasticity to seismic anisotropy. Earth and Planetary Science
867 Letters, 306, 33–45. https://doi.org/10.1016/j.epsl.2011.03.021

868 Wessel, P., Smith, W.H.F., Scharroo, R., Luis, J.F., & Wobbe, F. (2013). Generic mapping tools:
869 Improved version released. Eos, Transactions American Geophysical Union, 94, 409–410.
870 https://doi.org/10.1002/2013eo450001

871 Williams, Q., & Garnero, E. J. (1996), Seismic evidence for partial melt at the base of Earth's
872 mantle, Science, 273, 1528–1530.

873 Wysession, M.E., Bartkó, L., Wilson, J.B. (1994). Mapping the lowermost mantle using core–
874 reflected shear waves. J. Geophys. Res. 99 (B7), 13667–13684.

Figure 1.

a)

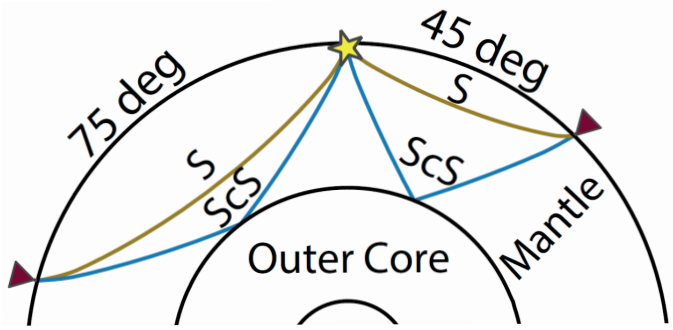
75 deg
45 deg
S
S
ScS
ScS
Outer Core
Mantle

b)

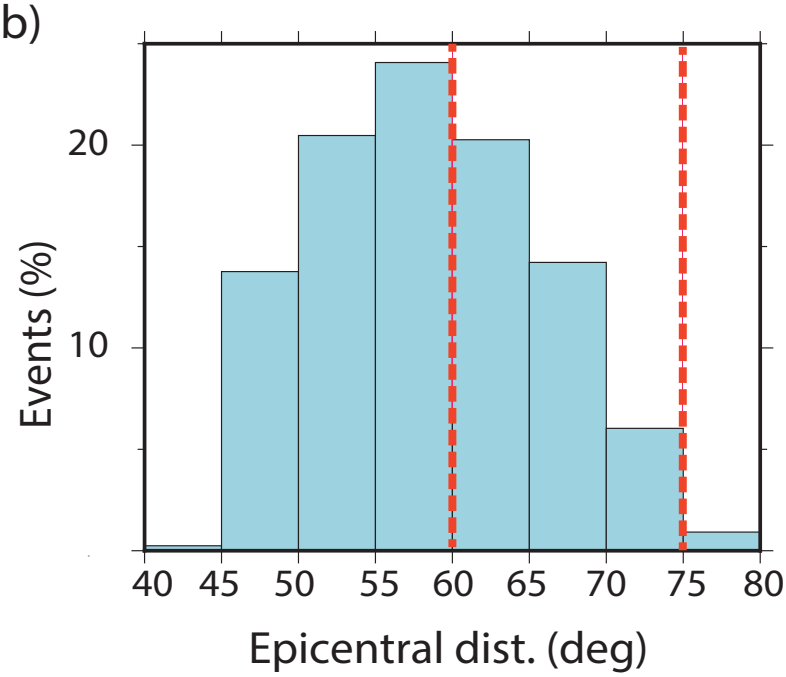
20
10
Events (%)
40
45
50
55
60
65
70
75
80
Epicentral dist. (deg)

Figure 2.

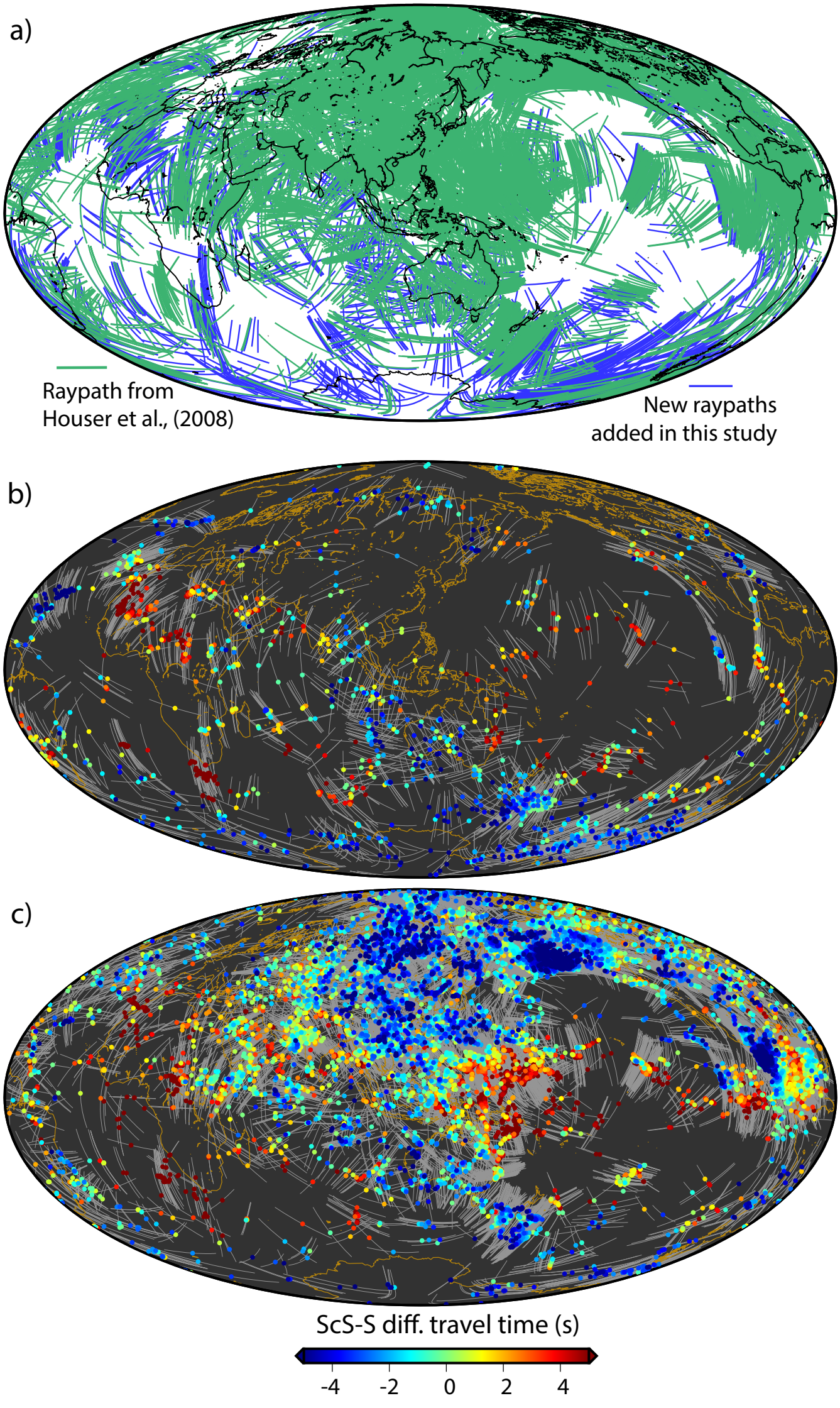
a)
Raypath from
Houser et al., (2008)
New raypaths
added in this study
b)
c)
ScS-S diff. travel time (s)
-4
-2
0
2
4

Figure 3.

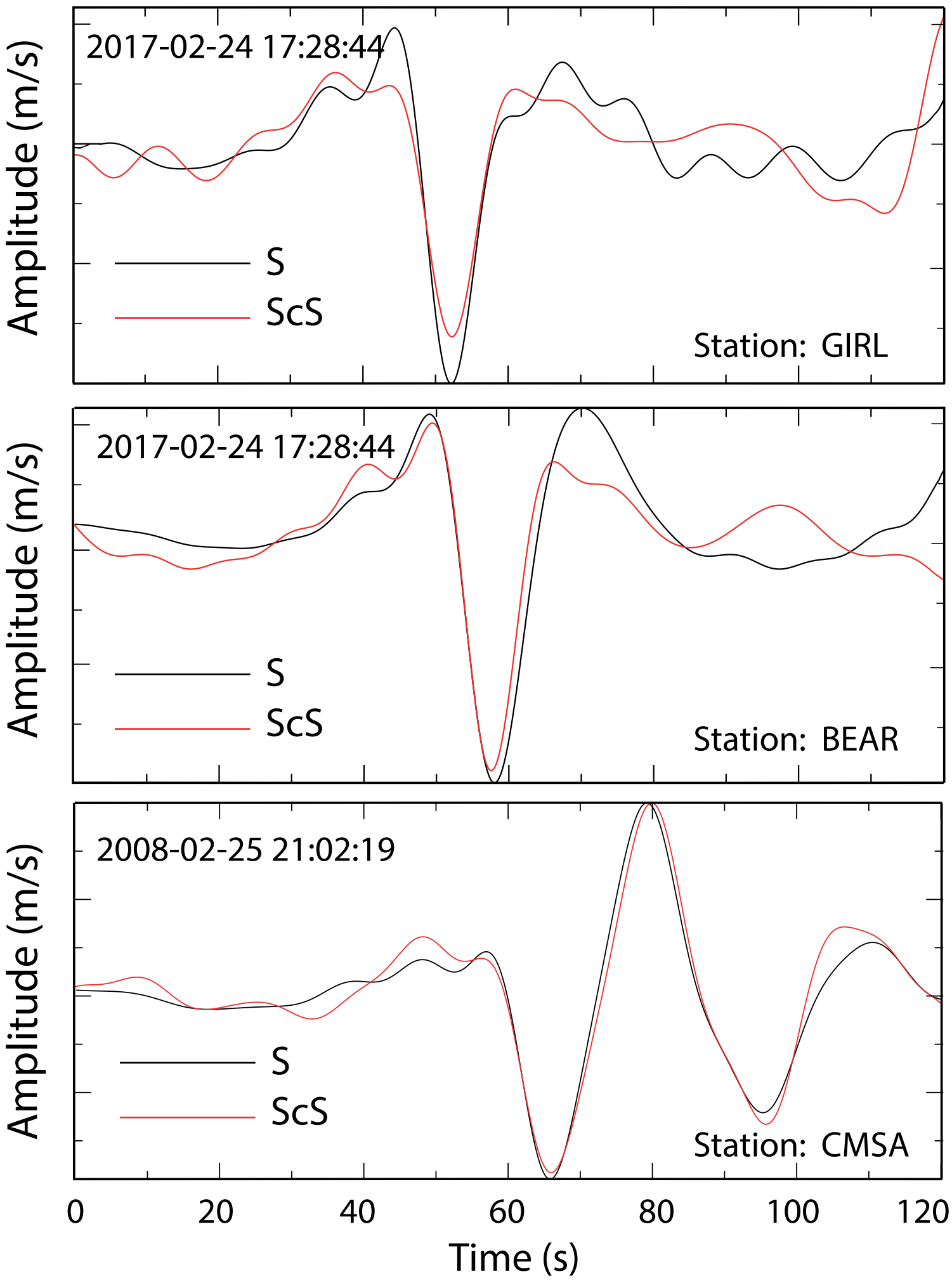
2017-02-24 17:28:44
S
ScS
Station: GIRL
Amplitude (m/s)
2017-02-24 17:28:44
S
ScS
Station: BEAR
Amplitude (m/s)
2008-02-25 21:02:19
S
ScS
Station: CMSA
Amplitude (m/s)
0
20
40
60
80
100
120
Time (s)

Figure 4.

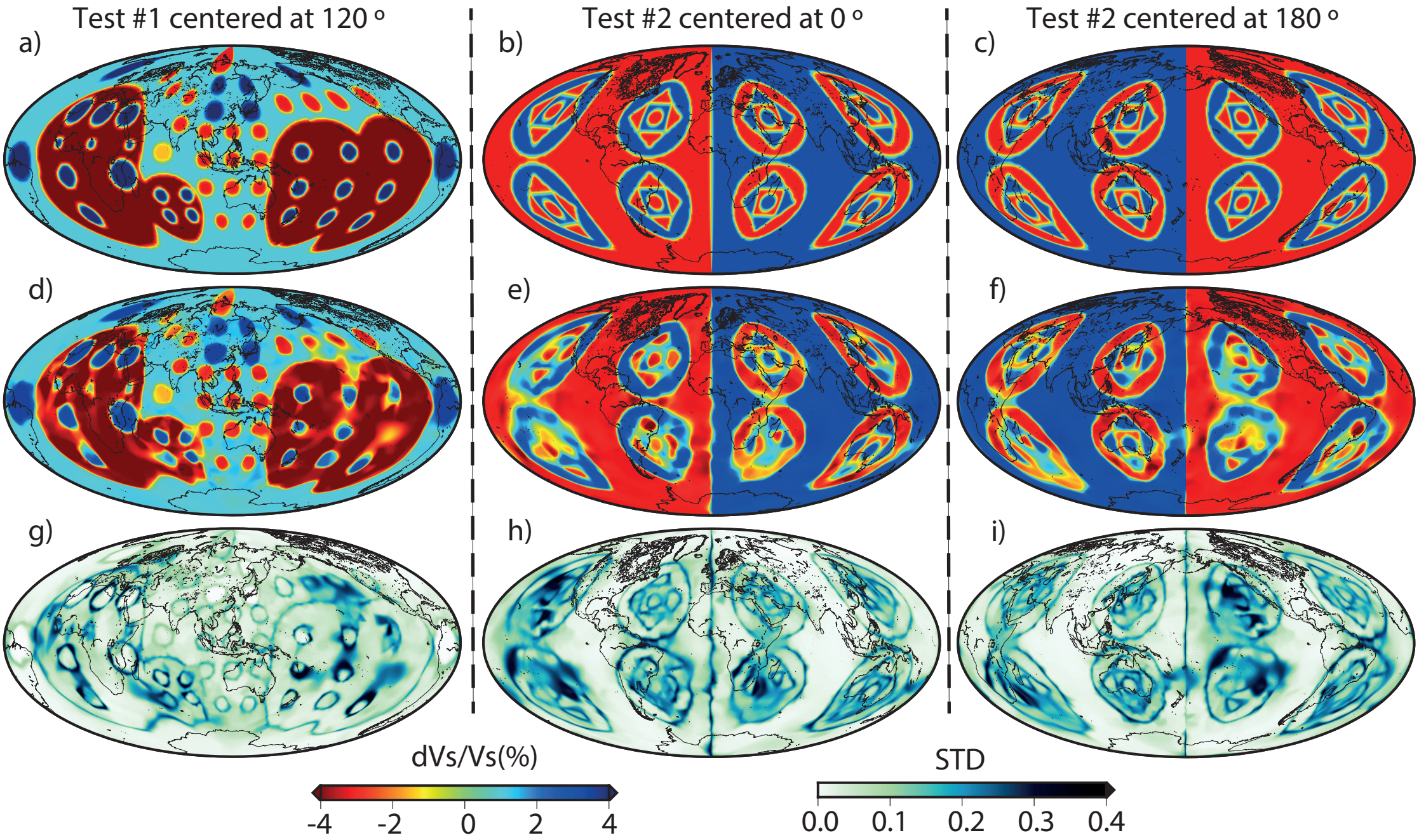
Test #1 centered at 120 °
Test #2 centered at 0 °
Test #2 centered at 180 °
a)
b)
c)
d)
e)
f)
g)
h)
i)
dVs/Vs(%)
-4
-2
0
2
4
STD
0.0
0.1
0.2
0.3
0.4

Figure 5.

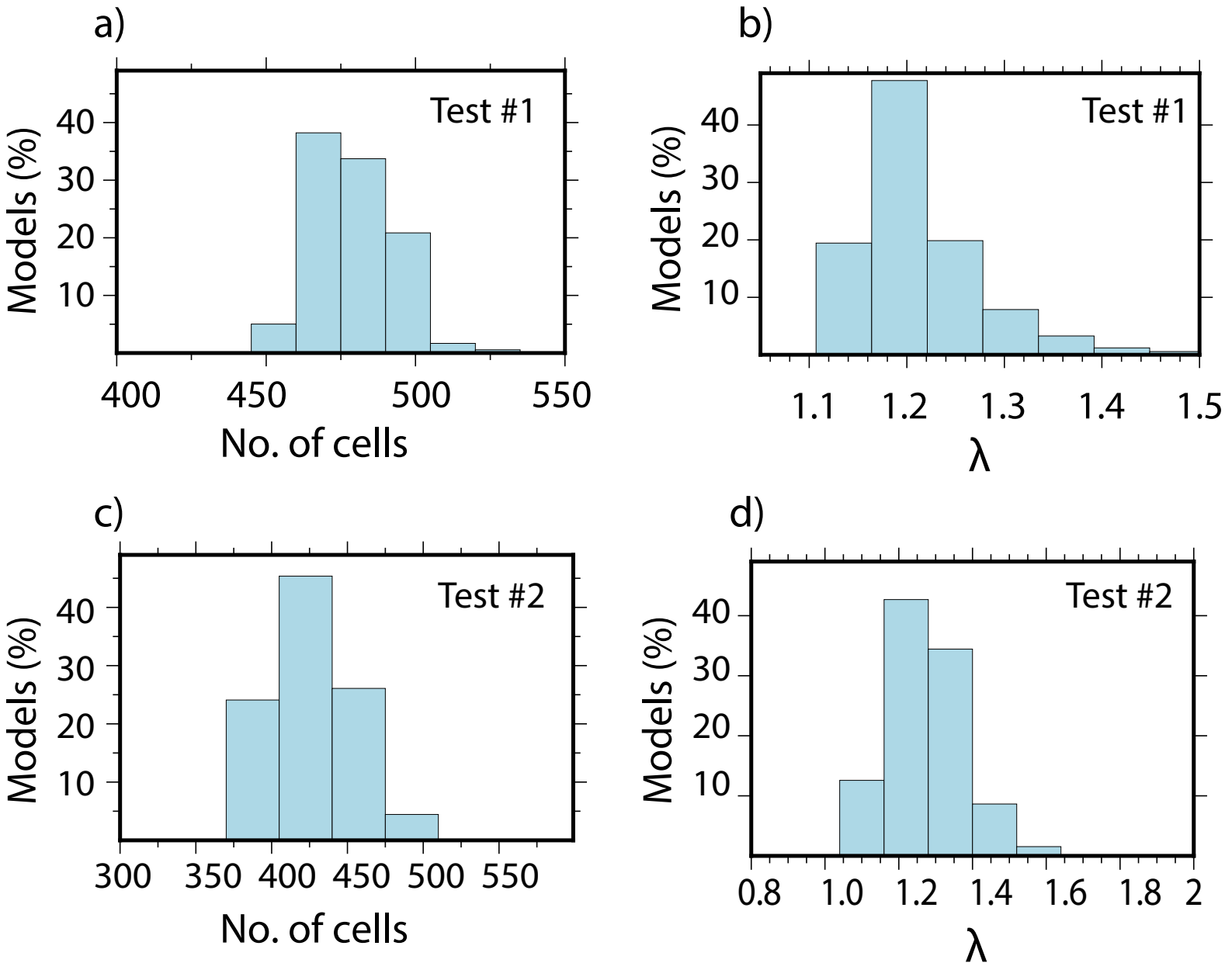
a)
Test #1
Models (%)
40
30
20
10
400
450
500
550
No. of cells
b)
Test #1
Models (%)
40
30
20
10
1.1
1.2
1.3
1.4
1.5
λ
c)
Test #2
Models (%)
40
30
20
10
300
350
400
450
500
550
No. of cells
d)
Test #2
Models (%)
40
30
20
10
0.8
1.0
1.2
1.4
1.6
1.8
2
λ

Figure 6.

Mantle corrected using TX2011

a)

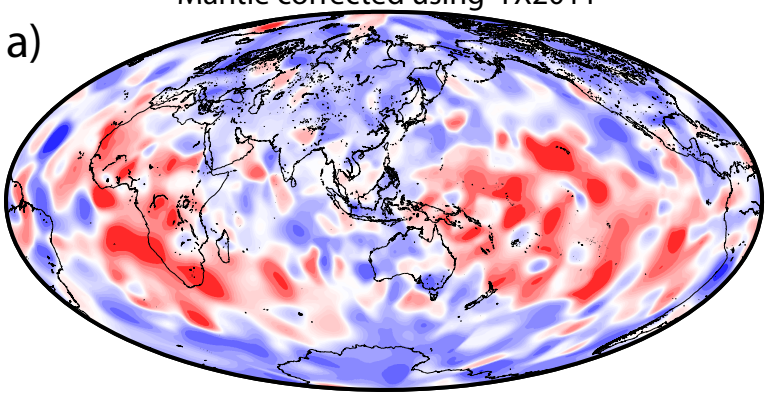

Mantle corrected using SEMUCB–WM1

b)

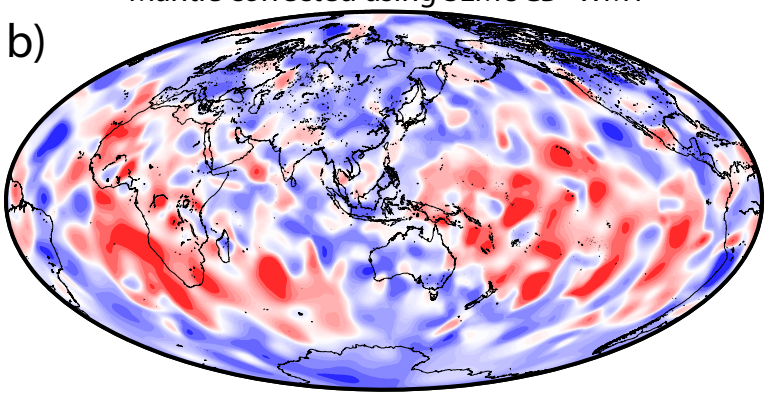

Mantle corrected using GyPSuM

c)

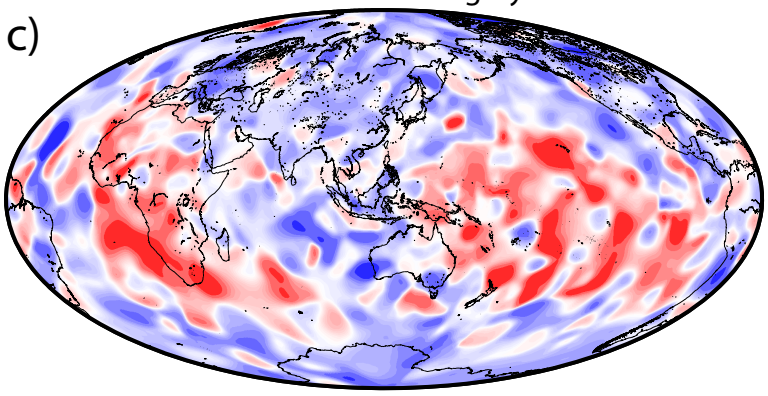

Mantle corrected using SAW642ANb

d)

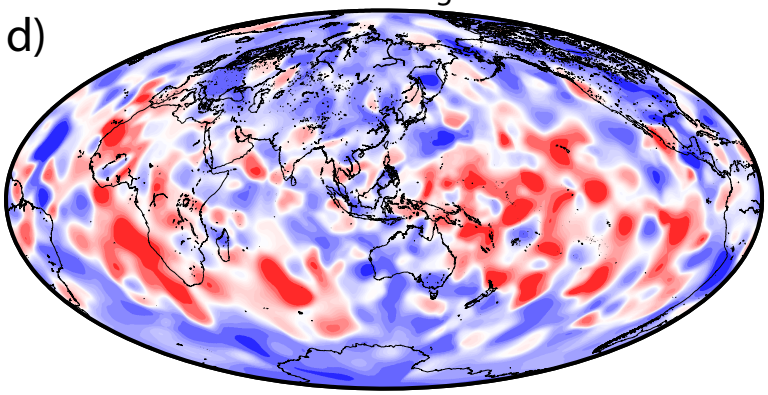

Mantle corrected using S362ANI+M

e)

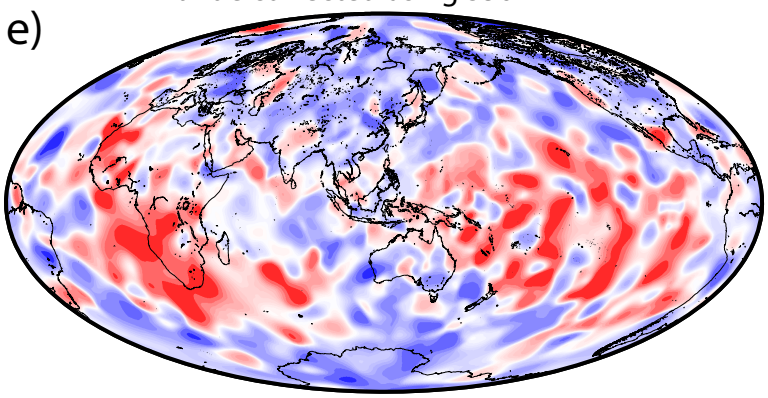

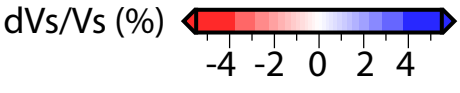

Figure 7.

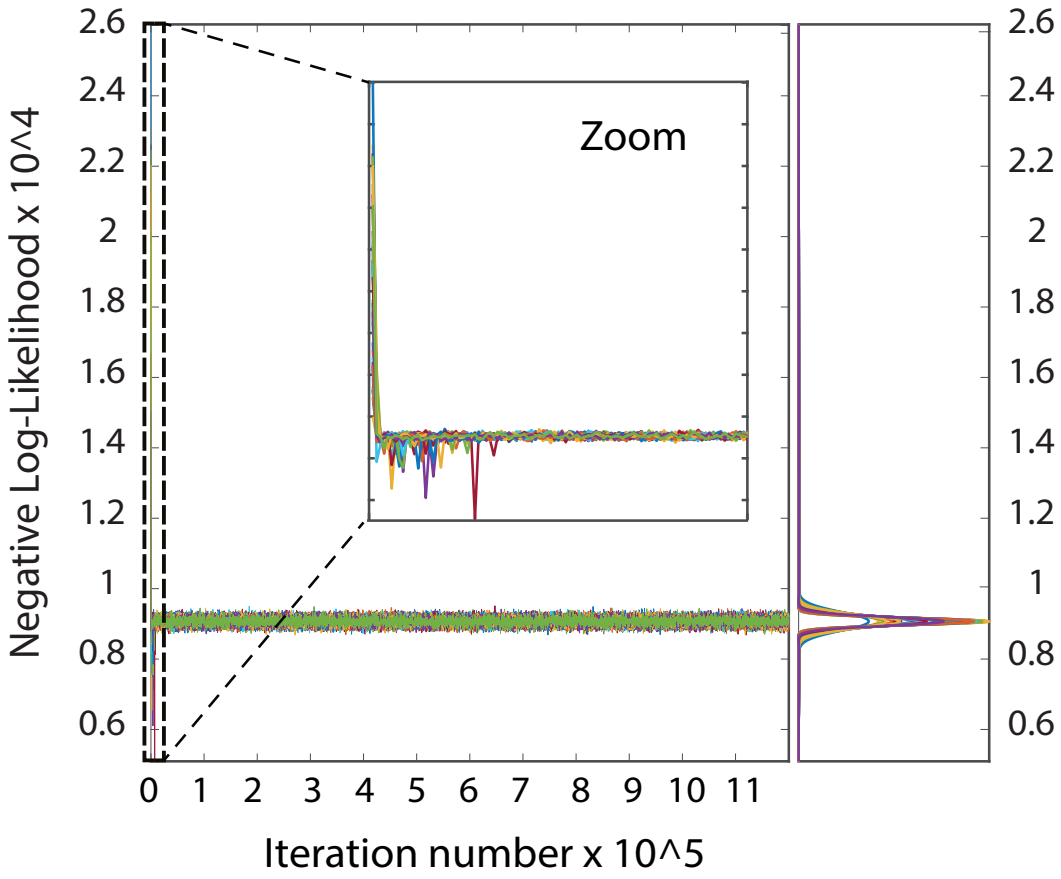
Zoom
Negative Log-Likelihood x 10^4
Iteration number x 10^5
2.6
2.4
2.2
2
1.8
1.6
1.4
1.2
1
0.8
0.6
0 1 2 3 4 5 6 7 8 9 10 11

Figure 8.

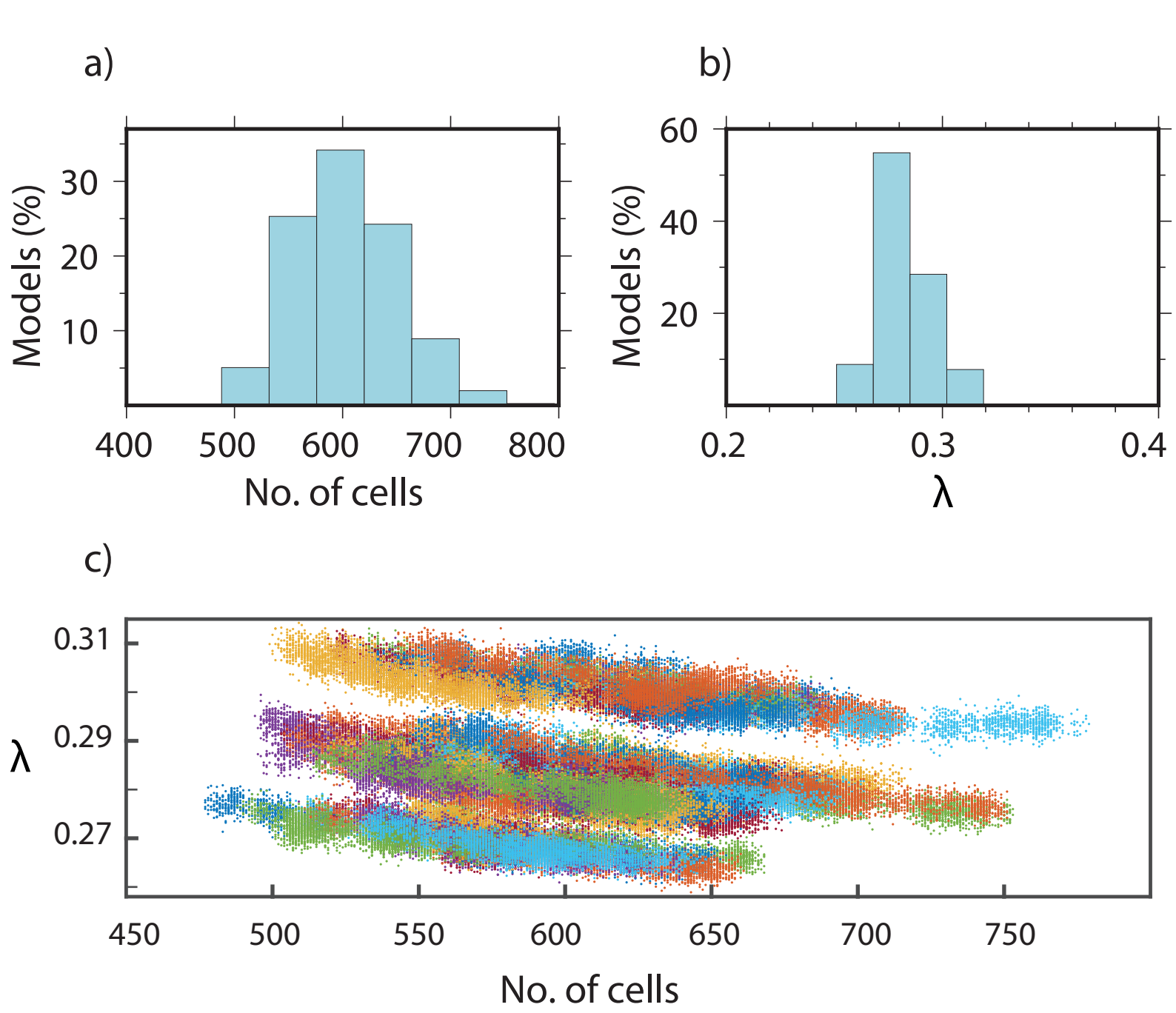
a)
Models (%)
30
20
10
400
500
600
700
800
No. of cells
b)
Models (%)
60
40
20
0.2
0.3
0.4
λ
c)
λ
0.31
0.29
0.27
450
500
550
600
650
700
750
No. of cells

Figure 9.

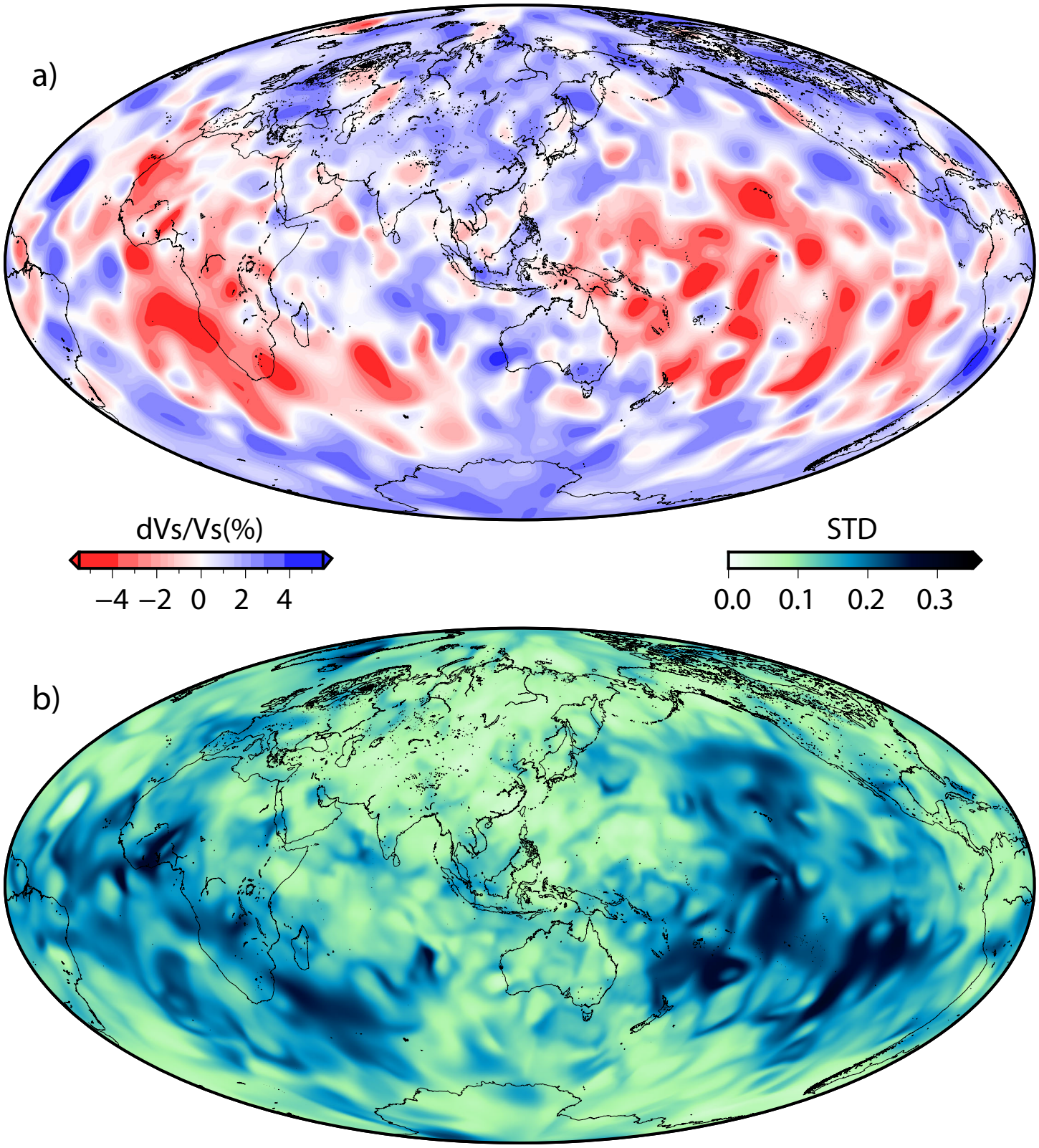
a)
dVs/Vs(%)
−4 −2 0 2 4
STD
0.0 0.1 0.2 0.3
b)

Figure 10.

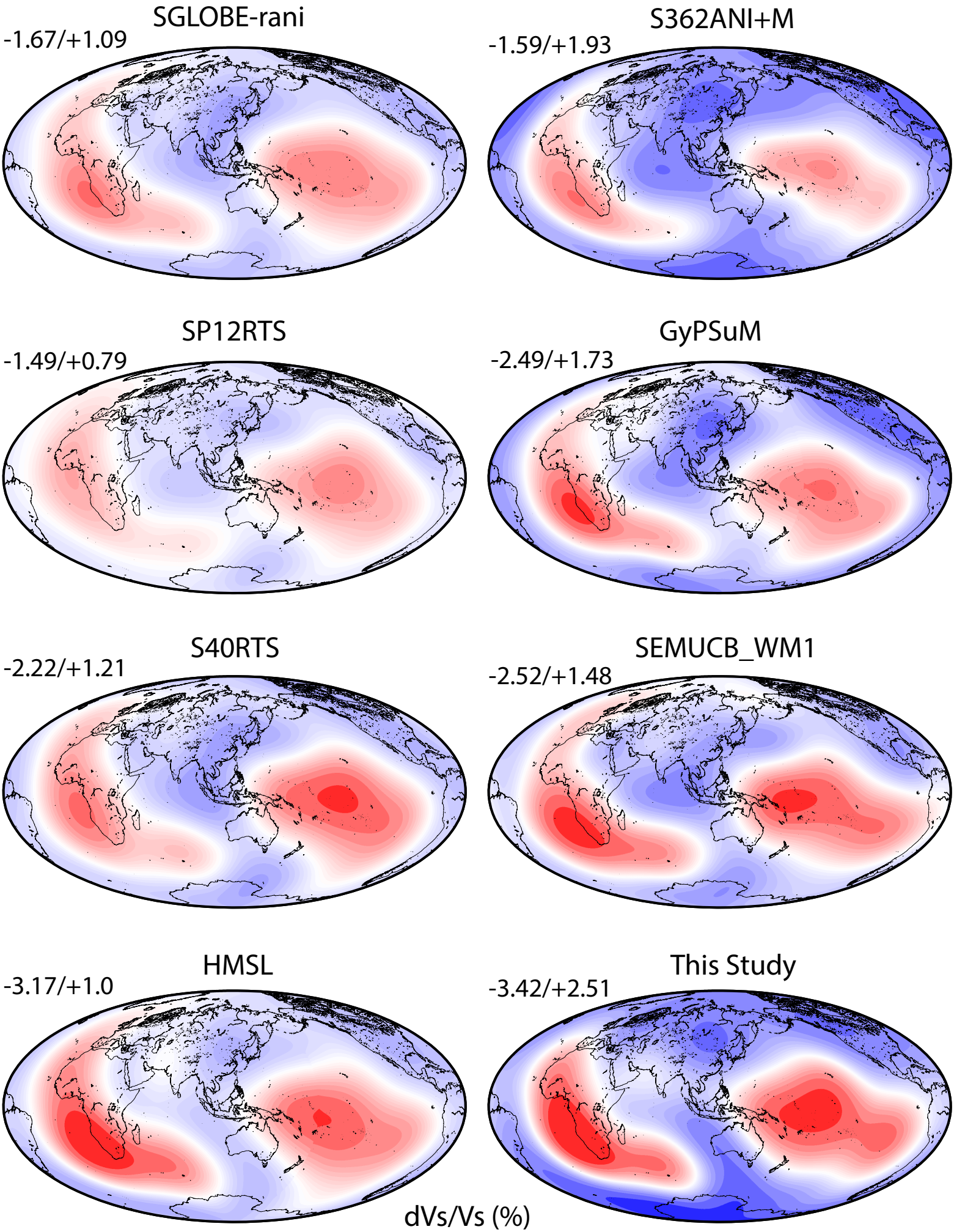
SGLOBE-rani
-1.67/+1.09
S362ANI+M
-1.59/+1.93
SP12RTS
-1.49/+0.79
GyPSuM
-2.49/+1.73
S40RTS
-2.22/+1.21
SEMUCB_WM1
-2.52/+1.48
HMSL
-3.17/+1.0
This Study
-3.42/+2.51
dVs/Vs (%)
-2
0
2

Figure 11.

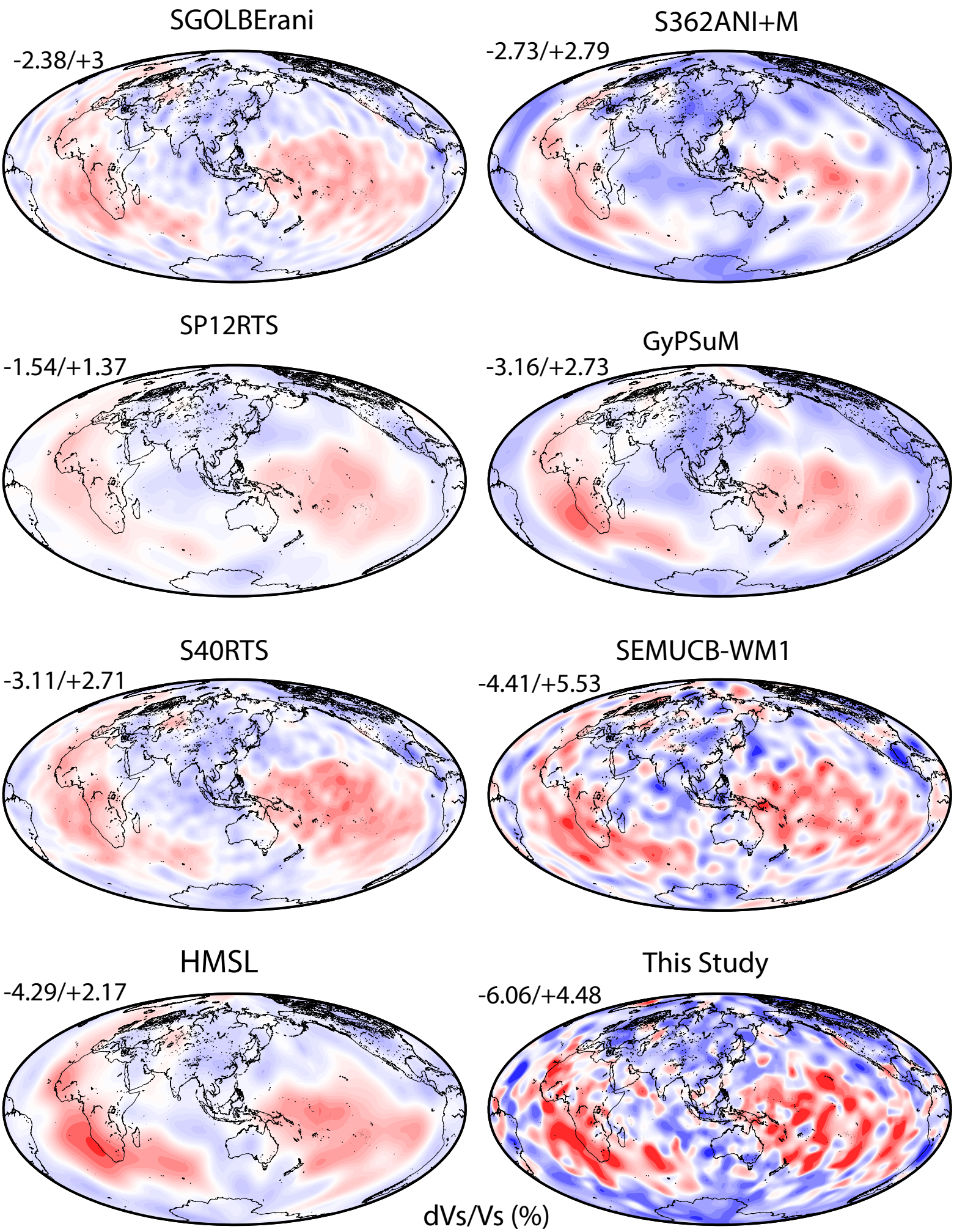
SGOLBErani
-2.38/+3
S362ANI+M
-2.73/+2.79
SP12RTS
-1.54/+1.37
GyPSuM
-3.16/+2.73
S40RTS
-3.11/+2.71
SEMUCB-WM1
-4.41/+5.53
HMSL
-4.29/+2.17
This Study
-6.06/+4.48
dVs/Vs (%)
-4
-2
0
2
4